CHALMERS
UNIVERSITY OF TECHNOLOGY

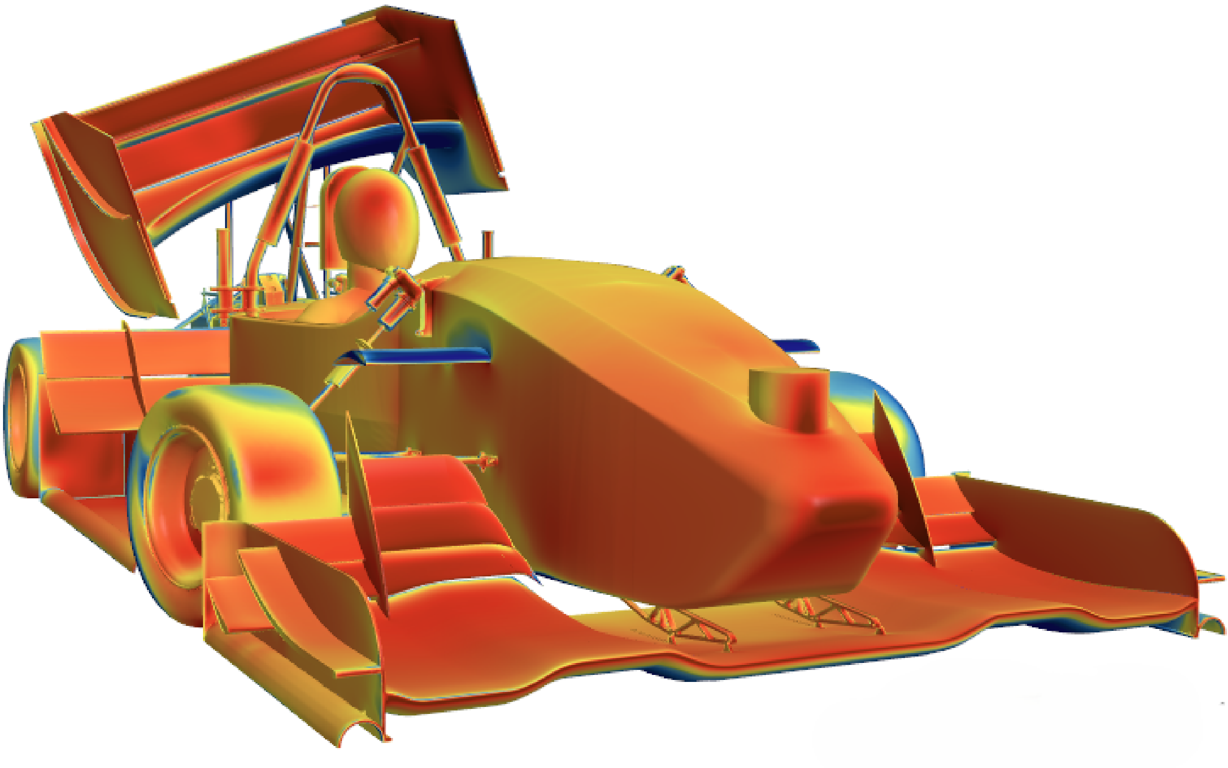

Aerodynamic evaluation of an active Rear Wing on a Formula Student Car

In collaboration with Chalmers Formula Student

Master's thesis in Mobility Engineering

GIANMARCO MANCINI

DEPARTMENT OF MECHANICS AND MARITIME SCIENCES
CHALMERS UNIVERSITY OF TECHNOLOGY
Gothenburg, Sweden 2025
www.chalmers.se

Master's Thesis in Mobility Engineering

Aerodynamic evaluation of an active Rear Wing in a Formula Student car

In collaboration with Chalmers Formula Student

GIANMARCO MANCINI

Department of Mechanics and Maritime Sciences
Division of Vehicle Engineering and Autonomous Systems
Chalmers University of Technology
Gothenburg, Sweden 2025

Aerodynamic evaluation of an active Rear Wing in a Formula Student car
In collaboration with Chalmers Formula Student
GIANMARCO MANCINI

Supervisor: Christian Svensson, Division of Fluid Dynamics
Examiner: Alexey Vdovin, Division of Vehicle Engineering and Autonomous Systems

Master's Thesis 2025
Department of Mechanics and Maritime Sciences
Chalmers University of Technology
SE-412 96 Gothenburg
Sweden
Telephone +46 31 772 1000

Cover: Pressure coefficient illustration of the CFS25 car "Svea" in a 20°-tilt rear wing configuration.

Typeset in LaTeX
Gothenburg, Sweden 2025

Aerodynamic evaluation of an active Rear Wing in a Formula Student car
In collaboration with Chalmers Formula Student
GIANMARCO MANCINI
Department of Mechanics and Maritime Sciences
Division of Vehicle Engineering and Autonomous Systems
Chalmers University of Technology

Abstract

Aerodynamic downforce is a crucial attribute in motorsports as it increases the normal load on a vehicle, pushing it to the ground and allowing to reach higher speed and stability in corners and other transient maneuvers. When it comes to Formula Student competitions, the large amount of cornering scenarios and the overall similarities between vehicles make downforce one of the main variables that can turn a normal car into a winning car, making a huge difference in all events.

This master's thesis explores the potential implementation of an active rear wing on the 2025 Chalmers Formula Student car and analyzes its effects over the behavior of the vehicle, aiming at stating whether this can be a way to enhance the car's performance and increase the team's winning chances in all events.

The project is carried over through Computational Fluid Dynamics simulations and vehicle dynamics calculations, and provides the reader with an overview of the consequences that tilting a wing has on a racing car.

Keywords: aerodynamics, downforce, cornering, formula student, rear wing, CFD, vehicle dynamics.

Preface

This report presents the outcome of my master's thesis project carried out at the Department of Mechanics and Maritime Sciences at Chalmers University of Technology during the spring of 2025. Being part of Chalmers Formula Student for two years, one of which as Aerodynamics Manager, made me develop an affection for the project, the people and our cars so deep that I wanted to spend the last semester of my academic career exploring and analyzing ways to potentially enhance our future cars' performances. Special focus has been put in making the material created and used in the development of this work suitable for the CFS Aerodynamics team and ready to use in both the remainder of the 2025 season and the upcoming ones, to help the team's design process and establish ourselves among the very best.

Acknowledgements

I want to deeply thank my examiner, Alexey Vdovin, Researcher in Vehicle Engineering and Autonomous Systems, for giving me the opportunity to carry out this project and providing me with everyhting I needed, even after working hours.

I am immensely grateful to my supervisor, Christian Svensson, PhD student in Fluid Dynamics, for his invaluable support and guidance not only in the development of this project, but also during my time at CFS. I owe you a lot.

I thank Björn Pålsson, Associate Professor in the Department of Mechanics and Maritime Sciences, and most importantly Head of the Chalmers Formula Student project (I hope it is the correct title, but you are the head anyways), for believing in me two years ago and making me live this amazing experience.

A special thanks goes to all my CFS24 friends, because thanks to you I have made memories that I will take with me forever, and the CFS25 team members, who I am so proud of having managed and seen creating a soon-to-be gem of a car.

I want to thank my family for always supporting me, my studies, and most importantly dealing with me during my studies. I hope I'll be able to pay you back.

I also want to thank my best friend, Chiara, who stood beside me during the ups and downs of my life in Sweden. You already know everything.

Finally, I thank Freja, the CFS24 car, my car, that gave me a place to be, five trophies to lift, and a career in Formula One. You would have deserved better luck. And even if you are now in pieces, I will always love you.

Gianmarco Mancini, Gothenburg, June 2025

List of Acronyms

Below is the list of acronyms that have been used throughout this thesis listed in alphabetical order:

4WD	Four Wheel Drive
AoA	Angle of Attack
CAD	Computer Aided Design
CFD	Computational Fluid Dynamics
CFS	Chalmers Formula Student
CoG	Center of Gravity
CoP	Center or Pressure
DF	Downforce
FDD	Front Downforce Distribution
FL	Front Left
FR	Front Right
FS	Formula Student
FSG	Formula Student Germany
FVM	Finite Volume Method
FW	Front Wing
LDD	Left Downforce Distribution
LIC	Line Integral Convolution
LLT	Lateral Load Transfer
LLTD	Lateral Load Transfer Distribution
RL	Rear Left
RR	Rear Right
RW	Rear Wing
SW	Side Wing(s)
VD	Vehicle Dynamics
VME	Vehicle Motion Engineering
WD	Weight Distribution

Nomenclature

Below is the nomenclature of parameters and variables that have been used throughout this thesis.

A	Area
a_y	Lateral acceleration
C_D	Drag coefficient
C_L	Lift coefficient
C_P	Pressure coefficient
D	Drag
f_i	External forces
F_x	Longitudinal load
F_y	Lateral load
F_z	Normal load
g	Gravitational acceleration
h	CoG height
k	Kinetic energy
L	Wheelbase
m	Mass
N	Normal load
P, p	Pressure
p_0	Stagnation pressure
R	Cornering radius
Re	Reynolds number
t	Time
T	Track width
u, v	velocity
v_c	Cornering speed

w	Track width
δ	Boundary layer thickness
ϵ	Rate of kinetic energy dissipation
μ	Dynamic viscosity
ρ	Density
τ	shear stress
ω	Specific rate of kinetic energy dissipation

Contents

List of Figures

List of Tables

1

Introduction

Formula Student (FS) is a student engineering competition in which universities compete with small-scale formula style cars designed and built by their students.
All aspects of the project, including design, manufacturing, testing, driving, funding and marketing are carried on by the students, with professional help only being allowed in an advisory setting.

All Formula Student competitions take place once a year inside the facilities of several race tracks, and feature four so-called dynamic events named Acceleration, Skidpad, Autocross, and Endurance (Trackdrive in Driverless classes).

1.1 Background

In this section, the aerodynamic package from Chalmers Fromula Student and the Centripetal Wing from Zenvo, which this thesis project is based on, are presented.

1.1.1 Aerodynamics at Chalmers Formula Student

Chalmers Formula Student, also referred to as CFS, is the FS team from Chalmers University of Technology; founded in 2002, it has been competing ever since, first with combustion cars and then, from 2015, with electric vehicles.
From 2022, cars from CFS also compete in the Driverless class; in this particular context the team achieved a first and second place at Formula Student Germany (FSG), in 2023 and 2024 respectively, and a third place at Formula Student East 2024. [1]

For the 2025 season CFS has presented their latest car, named Svea, featuring a Four Wheel Drive (4WD) electric driveline, a fully redesigned monocoque and an aggressive aerodynamic package.

The reason behind the presence of an aerodynamic package on race cars is to increase on-track performance by generating the so-called aerodynamic downforce, defined as a downward vertical force generated by aerodynamic devices that pushes the vehicle to the ground: the increase in normal load on the tires helps during braking and acceleration scenarios, and as a consequence a larger lateral tractive force can be produced enhancing cornering performance.

Svea features an evolution of the CFS24 aerodynamics package, keeping the same front wing (FW) and rear wing (RW); radical changes affect diffuser and side wings (SW), completely redesigned to improve ground effect and increase the overall downforce.
Each device is fully manufactured in carbon fiber for a combined weight of around the 10% of Svea's weight, thus providing performance with a limited impact on the total weight.

1.1.2 Zenvo's Centripetal Wing

Except for Acceleration, in the rest of FS events cars experience mostly cornering scenarios, as can be seen from the FSG 2024 Endurance track featured in Figure 1.1.

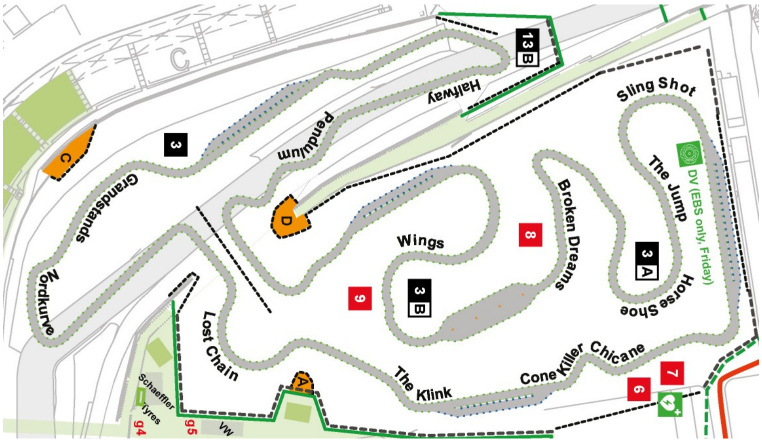

Figure 1.1: Endurance track from FSG 2024. [2]

When a vehicle takes a corner it experiences a Lateral Load Transfer (LLT), meaning that the tires closest to the curve center (called "inner tires" in this text) experience a decreased vertical load compared to the tires furthest away from the curve center (also "outer tires"); this can lead to larger tire wear, tire overloading and, ultimately, loss of traction at the rear.

To counteract this phenomenon, the Danish car manufacturer Zenvo has designed a special active rear wing, called Centripetal Wing. This technology was applied on their Zenvo TSR-S, where it acts to counteract the LLT: when taking a corner the inner side of the wing lifts so that, in the manufacturer's intentions, the load normal to the now tilted wing's plane creates a counteracting moment that keeps the inner wheels pushed to the ground.

It must be mentioned that the Centripetal Wing not only tilts around the longitudinal axis but also around the lateral, increasing its angle of attack in braking maneuvers; this feature is not considered in this study, where the rear wing is tilted only around the longitudinal axis.

According to Zenvo, at the maximum tilt of 20 degrees this system gives a consistent 30% Lateral Load Transfer shift while only losing 3% of the total downforce, meaning that the only thing changing would be where the load is applied, more than the actual amount of load which would be decreasing. [3]

The system has received general criticism within the automotive industry.
In particular, according to race engineer Jeff Braun's opinion, the introduction of the Centripetal Wing would anyway load the rear inner tire of the car, inducing lift on the opposite front outer tire similarly to a skateboard, and therefore generating understeer. [4]

1.2 Purpose

The intent of this project is to simulate, analyse and evaluate the effect that rotating the rear wing of the CFS25 car about its longitudinal axis would have on performance compared to the current fixed design, both in terms of downforce and time gained in the Skidpad event, given the differences between a Formula Student vehicle and a road car featuring a rear wing like the Zenvo TSR-S.

1.3 Goals

The main goal of this project is to evaluate the optimal Rear Wing tilt angle, which is the one resulting in the fastest laptime, for

- a Skidpad corner, with a radius of 8.5 m;
- the sharpest corner allowed by Formula Student regulations, with a radius of 4.5 m; [5]
- the widest corner CFS has recorded data for, with a radius of 18 m.

It will then be evaluated whether it would be possible or not to tune the system for the Skidpad event only, or for other dynamic events like Autocross or Endurance, based on the results from the first phase of the study.

Modified versions of the CFS tire model will be applied to each scenario to evaluate in which conditions this system would be more or less beneficial.

1.4 Limitations

This project does not resemble real-world conditions for multiple reasons, which are discussed in this section.

First, the system will not be manufactured, as it would require an entirely new rear wing. Therefore it will not be implemented on Svea, which means that it will not be tested on-track or in a physical Wind Tunnel, and it will only be judged through simulations.

As will be explained in more detail in Chapter 3, the CAD model of the car used for simulations presents several simplifications that eventually make results slightly differ from what would be tested in reality; to simplify calculations, the driving condition is assumed to be steady-state cornering, and several other assumptions are made on the vehicle dynamics models used.

To implement the tilting function of the rear wing, a new set of mountings including two actuators would be needed; since this study does not feature any analysis of the actuation system used by Zenvo, simulations and results do not take into account weight increase and center of gravity shift coming from this.

Different scenarios are tested using data recorded on the CFS24 car, Freja; these data refer to 2024 competitions, where Freja mounted 6” tires, and on-track test sessions, performed with both the old tires and the new 7.5” tires (also referred to as LC0 7.5 in this text) that will be mounted on Svea.
This difference means that parameters such as body slip, roll and steering angles, and even the speed achieved in the different cornering scenarios, used in this project may not reflect realistic conditions; therefore, results coming from this study cannot be used to directly compare Svea with Freja.

As previously mentioned, only the tilt around the longitudinal axis is tested on Svea’s rear wing while the rotation around the lateral axis is ignored; this is done to simplify the study focusing on one function only, as implementing two different functions would require much more time and resources than those available.

The same reasons led to the absence of a deep mesh study, which might be the source of small deviations in some results even though the main trends, as will be shown in Chapter 4, are still respected.

2

Theory

Theoretical laws and physical phenomenons, needed for a proper understanding of this thesis project, are presented in this chapter.

Vehicle dynamics concepts are discussed first, followed by fluid dynamics and aerodynamics principles in Section 2.2.
A description of aerodynamic wings and the expected behavior of CFS' rear wing in this study is given in Sections 2.3 and 2.4, followed by a presentation of the implications coming from a cornering scenario in Section 2.5.
Section 2.6 features a discussion about the interactions occurring between aerodynamics and vehicle dynamics, then a brief overview of the turbulence models used to set the CFD environment is given in Section 2.7.

2.1 Vehicle Dynamics Theory

This section presents vehicle dynamics concepts and mechanisms, from the most relevant ones to those needed for a complete understanding of the content.

2.1.1 Lateral Dynamics

In a steady-state cornering scenario, a car experiences a load transfer from the inner to the outer side.
This mechanism is explained here for a generic car, while Section 2.6 features a discussion about how this is influenced by aerodynamic forces for a race car.

The same scenario presented in this project, with a generic car turning left, is shown in Figure 2.1, where ma_y is a fictive force applied at the Center of Gravity (CoG), defined as the point where also the total weight (mg, where m is mass and g is gravitational acceleration) of the vehicle can be considered to be applied, and h is the vertical distance between CoG and the ground; l and r subscripts indicate left and right, while w represents the track width of the vehicle, which is the distance between the centerlines of the left and right tire: this can be different for front and rear axles, but it is not of importance in this discussion and it is however constant for CFS25.

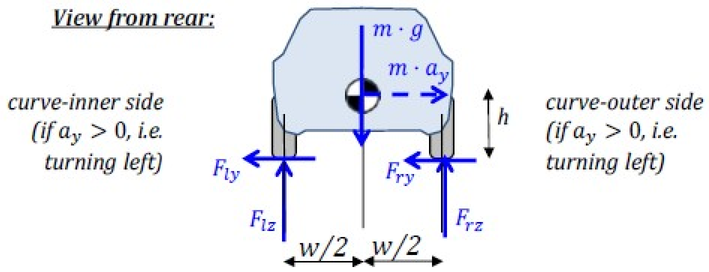

Figure 2.1: Generic vehicle turning left, rear view.

The moment equilibriums around left and right contacts with the ground give:

$$F_{rz} = m\left(\frac{g}{2} + a_y \frac{h}{w}\right) \tag{2.1}$$

$$F_{lz} = m\left(\frac{g}{2} - a_y \frac{h}{w}\right) \tag{2.2}$$

The different signs in the equations above show that lateral acceleration a_y causes an increase in the normal load on the outer side and a decrease on the inner side. [6]

2.1.2 Tire Load Sensitivity

Tire Load Sensitivity defines the behavior of tires under load.

Since the relationship between friction and normal load is not perfectly linear, tires will generate more grip as load increases up to a certain point, after which grip will continue growing slowly.
Eventually a point of overloading will be reached, after which no additional grip will be generated even if normal load increases, and instead resulting in a decrease of friction as load increases.

2.1.2.1 CFS' Tire Model

The tire model in Figure 2.2, developed and tested by the team, can be translated into the following formula in order to calculate the lateral force produced by each tire:

$$F_{y_{FL,FR,RL,RR}} = F_{z_{FL,FR,RL,RR}} * (-0.0003109 * F_{z_{FL,FR,RL,RR}} + 1.78027) \tag{2.3}$$

The presented model shows that for Freja, at least between 200 and 2000 N, adding normal load to any of the four tires results in a linear decrease of friction coefficient; the lateral load generated depends on how balance is distributed, as will be better illustrated in section 2.6.

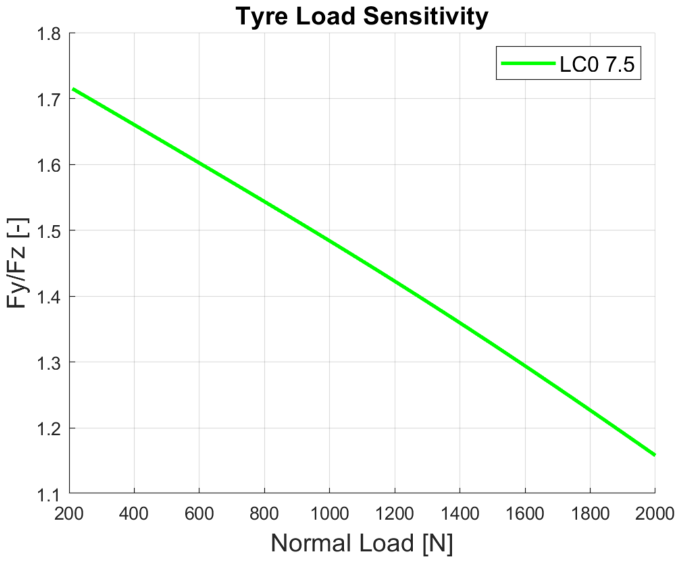

Figure 2.2: Tire model used by CFS, with the friction coefficient on the y axis.

2.1.3 CoG influence over steering behavior

In general, the front and rear axles together share the total vertical load generated by the car's weight.
A CoG that is closer to the front axle than to the rear can be defined as forward placed and makes a vehicle understeer, due to tire load sensitivity: the front tires get overloaded and lose grip, so that the car follows a larger path mostly driven by the rear tires.
In the opposite way, a CoG shifted rearwards causes oversteering, as the rear tires get overloaded and lose grip, while the front of the car tends to turn towards the corner.
A CoG placed in the middle balances front and rear, providing an easier neutral handling.

Unwanted behaviors caused by the position of the CoG can be counteracted by a proper distribution of aerodynamic downforce, and this will be explained in more detail in Section 2.6.

2.1.4 Contact Patch Deformation

The surface of a tire when in contact with the ground is named Contact Patch, and it changes during maneuvers that induce different forces on the tire, due to the rubber deforming over the ground surface.
This deformation can heavily affect grip, in particular during transient maneuvers such as braking or cornering.

2.1.5 Steering Angle

The Steering Angle is the angle between the longitudinal axis of the car and the longitudinal axis of a wheel.

CFS is currently using the Anti-Ackermann steering geometry, where the front outer wheel turns more than the inner; this is a commonly used geometry in high-performance cars, improving tire slip angle and therefore grip.

2.1.6 Body Slip Angle

The Body Slip Angle is the angle between the longitudinal axis of the car and the direction of its velocity vector, and it is therefore induced by the yaw moment (rotation around the vertical axis) experienced by the car during a corner.

2.1.7 Roll Angle

During a corner, the outer tires being more loaded than the inner ones causes the car to lean to the outside, and the Roll Angle is the measurement of this rotation.

2.1.8 Ride Height

Ride height, also referred to as ground clearance in this project, is the vertical distance between the lowest point of the chassis (or the sprung mass) and the ground. According to the FSG 2025 regulations, ground clearance must be at least 30 mm already accounting for a seated driver.

2.2 Fluid Dynamics Theory

Fluid dynamics are discussed here, starting with principles and parameters, followed by key dimensionless parameters.

2.2.1 Laws and Equations

This section gives an overview of the basic principles and laws of fluid dynamics.

2.2.1.1 Continuity Equation

The continuity equation describes the principle of mass conservation, and in particular it relates the speed of flow through a certain section to the area of the section. Its differential form is

$$\frac{\partial \rho}{\partial t} + \nabla \cdot (\rho \vec{v}) = 0 \tag{2.4}$$

For incompressible flows it simplifies to

$$\nabla \cdot \vec{u} = 0 \tag{2.5}$$

meaning that the divergence of the velocity field is zero everywhere.

2.2.1.2 Navier-Stokes Equations

The Navier-Stokes equations are partial differential equations expressing the principle of momentum conservation for Newtonian fluids; they can be seen as the application of Netwon's second law to fluids, and are defined as

$$\rho\left(\frac{\partial\vec{v}}{\partial t}+(\vec{v}\cdot\nabla)\vec{v}\right)=-\nabla p+\mu\nabla^2\vec{v}+\rho\vec{g} \tag{2.6}$$

2.2.1.3 Bernoulli's Equation

In fluid dynamics, the pressure that a fluid that is not moving exerts on a surface, generating normal forces on it, is defined as static pressure; the kinetic energy of the fluid is instead defined as dynamic pressure.
The sum of static and dynamic pressure is defined as stagnation (or total) pressure and represents the flow pressure if the absence of losses would allow to reversibly convert all the dynamic pressure into static pressure.
This is true for steady, inviscid, incompressible flows, and it can be described by the Bernoulli's Equation defined as

$$p+\rho\frac{v^2}{2}=p_0 \tag{2.7}$$

where

- p is the static pressure;
- $\rho\frac{v^2}{2}$ is the dynamic pressure;
- p_0 is the stagnation pressure

The Bernoulli's Equation represents the main principle behind the design of diffusers and airfoils.

2.2.1.4 Boundary Layer Theory

When a fluid flows around a body, a thin layer of fluid immediately close to the surface gets formed: this is called boundary layer.
The boundary layer is defined as the region where the flow is driven by viscosity and the flow velocity is up to 99% of the free-stream velocity, which defines the layer's thickness; the boundary condition at the wall is a no-slip condition, meaning that the flow velocity on the surface is zero.

The boundary layer flow on an airfoil starts as laminar, defining a smooth laminar boundary layer which generates a limited amount of drag; as its thickness increases with the flow traveling from the leading edge, at a certain point the flow transitions to a turbulent condition, causing the generation of a turbulent boundary layer characterized by a larger drag generation, but less incline to separate. The relation between thickness and Reynolds Number (Re, defined in Section 2.2.2) can be described as follows:

$$\frac{\delta}{x} = \begin{cases} \frac{5}{Re_x^{1/2}}, & 10^5 < Re_x < 10^8, \text{ Laminar flow} \\ \frac{0.16}{Re_x^{1/7}}, & Re_x > 10^8, \text{ Turbulent flow} \end{cases} \tag{2.8}$$

The fluid flowing outside the boundary layer can be considered free-stream, as viscosity can be neglected and the presence of the body has no effect on the flow.

Figure 2.3 represents key parameters of a boundary layer for a fluid flowing in a 2D channel, where H is the distance between the two plates delimiting the domain and u is the velocity of the flow.

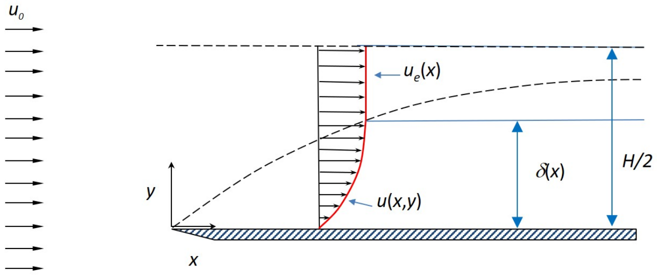

Figure 2.3: Key parameters of a boundary layer. [7]

2.2.1.5 Boundary Layer Separation

Boundary layer (or flow) separation occurs when a fluid flows towards an increasing pressure, thus in a condition of adverse pressure gradient, and the boundary layer loses speed up to the point where it begins to flow in the opposite direction.
This results in formation of a recirculation zone, increased pressure drag, reduced lift (or downforce) and possible stall; vortices, in particular, might generate vibrations leading to structural failures for certain frequencies.

An illustration of this phenomenon is given in Figure 2.4, where the last case shows the reversed flow.

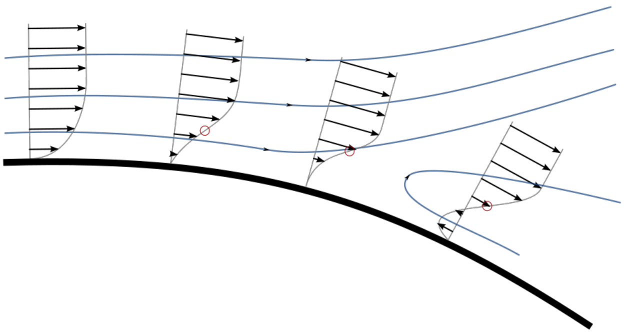

Figure 2.4: Velocity profile in a separated boundary layer. [8]

2.2.2 Dimensionless parameters

This section presents dimensionless parameters relevant in fluid dynamics.

2.2.2.1 Reynolds Number

The Reynolds number represents the ratio between inertial and viscous forces in a Newtonian fluid and can be written as

$$Re = \frac{\rho u L}{\mu} \tag{2.9}$$

2.2.2.2 Lift Coefficient

The lift coefficient is defined as

$$C_L = \frac{L}{\frac{1}{2}\rho v^2 A} \tag{2.10}$$

and describes the ability of a body to generate lift in a fluid.

2.2.2.3 Drag Coefficient

The drag coefficient is defined as

$$C_D = \frac{D}{\frac{1}{2}\rho v^2 A} \tag{2.11}$$

and describes the drag generation of a body in a fluid.

2.2.2.4 Pressure Coefficient

The pressure coefficient is defined as

$$C_p = \frac{p - p_\infty}{\frac{1}{2}\rho v_\infty^2} \tag{2.12}$$

and relates the static pressure on a certain point of the surface of a body to the static pressure of the free stream.
Its minimum value is theoretically $-\infty$, while its maximum for incompressible flows is $+1$, which corresponds to the stagnation pressure.

2.3 Aerodynamic Wing Theory

A discussion over the main characteristics of airfoils is presented in Section 2.3.1, while Section 2.3.2 features an overview of the rear wing design used by CFS.

2.3.1 Airfoil Theory

A typical motorsports wing can be seen as an upside-down airplane wing, with the lower side of the airfoil representing the suction side: the airflow below the airfoil gets accelerated and creates a low pressure zone, according to Bernoulli's law, which leads to downforce generation.
An illustration of an airfoil in a typical airplane configuration, with its defining nomenclature, is shown in Figure 2.5.

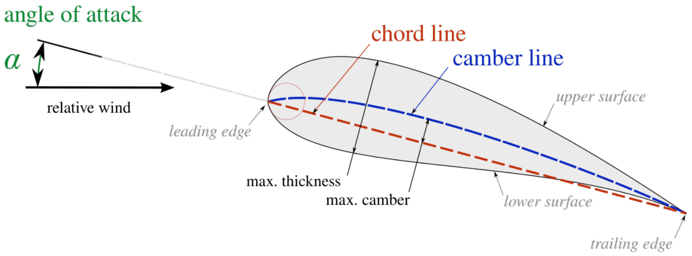

Figure 2.5: Airplane airfoil, with nomenclature. [8]

The leading edge is the point, at the front of the airfoil, with minimum radius; the trailing edge is the farthest point from the leading edge, located at the back.

The chord line is the straight line connecting leading and trailing edge, it defines the angle of attack (AoA) and its length, named chord length, is a defining parameter for an airfoil.

The mean camber line is the locus of points equidistant from the lower and upper surfaces; airfoils can be defined as high- or low-camber, based on the large or small curvature of their camber line.
High-camber airfoils can produce more lift - or downforce, in car applications - at a given AoA compared to low-camber airfoils, but they have a lower critical AoA, meaning that they tend to stall sooner as the AoA increases.

Thickness can be defined as the distance between lower and upper surface in the direction perpendicular to the camber line, as for the American convention, or to the chord line, as for the British convention.

Camber and thickness are also defining parameters for an airfoil.

The concave surface, which is the lower in the figure, corresponds to the pressure side, while the convex surface denotes the suction side: in this configuration the airfoil produces lift, while it produces downforce when the airfoil is placed upside down and the suction side ends up on the lower surface.

2.3.2 Multi-element Rear Wing design in CFS

The rear wing represents the rearmost aerodynamic device mounted on a race car, and it generates around the 30% of the total downforce.

For the rear wing, CFS uses a multi-element design composed of a main wing and two rear flaps; an additional multi-element overwing composed of two flaps is placed above the main wing.
Two endplates are mounted on the sides to prevent unwanted vortex generation from pressure to suction side of every element.

The preference for multi-element wings comes from the need for high downforce generation and adjustability of devices in those motorsports classes where advanced aerodynamic solutions are permitted, i.e. Formula One, Le Mans Prototypes and, of course, Formula Student cars.

Splitting a device into two or more elements allows to re-energize the air in the boundary layer, thus delaying separation and reducing turbulence.
This allows for higher angles of attack and therefore larger amounts of downforce generated, while keeping the drag generation relatively low compared to high-AoA single-body designs.
The rear wing from CFS25 is presented in the right picture of Figure 2.6, while the left is a Line Integral Convolution picture showing the airflow around its elements, where blue and yellow denote low- and high-speed air respectively.

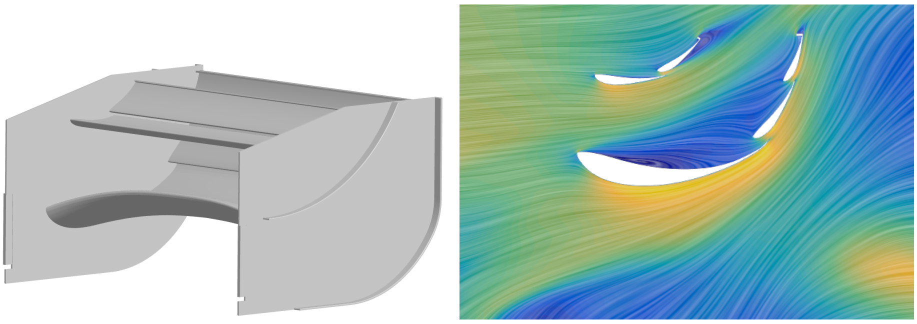

Figure 2.6: RW CAD model (left) and flow around it (right) for a no-tilt configuration in a cornering scenario.

Due to being placed at the rear of the car, the rear wing is largely influenced by what happens in front of it.
The airflow that the rear wing encounters depends primarily on front wing and side wings, but there is a strong interaction with the air expansion from the diffuser as well.
Bodies placed directly in front of it, like the Main Hoop as an example from FS cars, are another source of disturbance.

However, due to the fact that in aerodynamics all bodies influence others, the rear wing can also be a disturbance for other devices, changing how air is extracted from them; this mechanism requires teams to develop their aerodynamic package as a whole, considering all implications of every design change, in order to best utilize every device.

2.4 Expected Rear Wing downforce behavior

This project is based on tilting the rear wing around the longitudinal axis of the car; Figure 2.7 shows the normal load decomposition on the wing in a generic tilted configuration.

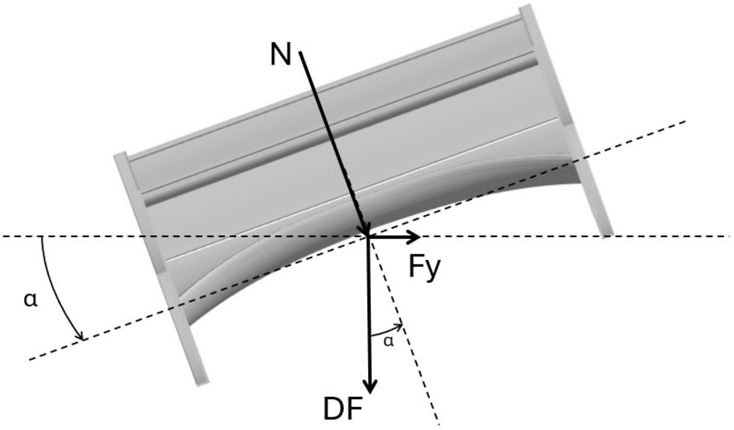

Figure 2.7: Load decomposition on a tilted CFS25 rear wing.

In the picture, N represents the load normal to the wing's plane, that in a horizontal setup would be called Downforce; α represents the wing's tilt angle.

Considering the Rear Wing alone, from a merely theoretical perspective, it is expected to see a reduction of the load normal to the ground as the wing gets tilted caused by the decomposition of N in a vertical force, DF, that is Downforce itself, and in an horizontal force, F_y, according to the following formula:

$$DF = Ncos(\alpha) \tag{2.13}$$

$$F_y = Nsin(\alpha) \tag{2.14}$$

However, as mentioned in the previous section, the airflow around the rear wing is strongly dependent on other aerodynamic devices installed on the vehicle: this means that theoretical expectations might not be met at certain configurations, due to the complexity of the aerodynamics of a race car.

This project is therefore based on the induction of a Lateral Load Transfer shift towards the inner side of the car and on the analysis of the interactions between the different aerodynamic devices mounted on it, in order to assess whether this could result in an improved overall behavior of Svea in cornering scenarios.

2.5 Cornering Aerodynamics

When a car is cornering, its aerodynamics change in different ways. The scenario is equivalent to air following a curved path around the vehicle: this means that the air velocity vectors are different at different distances from the center of the corner, and especially from the left to the right side of the car.

This leads to different consequences.

2.5.0.1 Curved Drag

The first implication is that drag needs to be calculated in a different way.
Curved Drag is now calculated as

$$D = (PA_x + \tau_x|A|)\, cos\xi + (PA_y + \tau_y|A|)\, sin\xi \tag{2.15}$$

where:

- P, pressure
- A, area
- τ, shear stress
- ξ, angle between the point where the flow is parallel to the vehicle and the center of the corner

This calculation is done for every cell in the domain, and the different values contribute to the total curved drag force. [10]

2.5.0.2 Drag and Downforce

The fact that aerodynamic devices are usually optimized for straight-line driving might cause them to generate uneven drag and downforce when surrounded by curved air.

In this condition, the amount of drag and downforce generated can increase and decrease depending on various factors, and larger separations can occur on devices that were designed for straight airflows.

Figure 2.8 shows a comparison between two simulations performed during the development of this project, where the same car configuration is tested in the Skidpad corner scenario on the left and in the Sharp corner scenario on the right.
Both pictures are captured on a plane normal to the ground, located 6 cm above it.

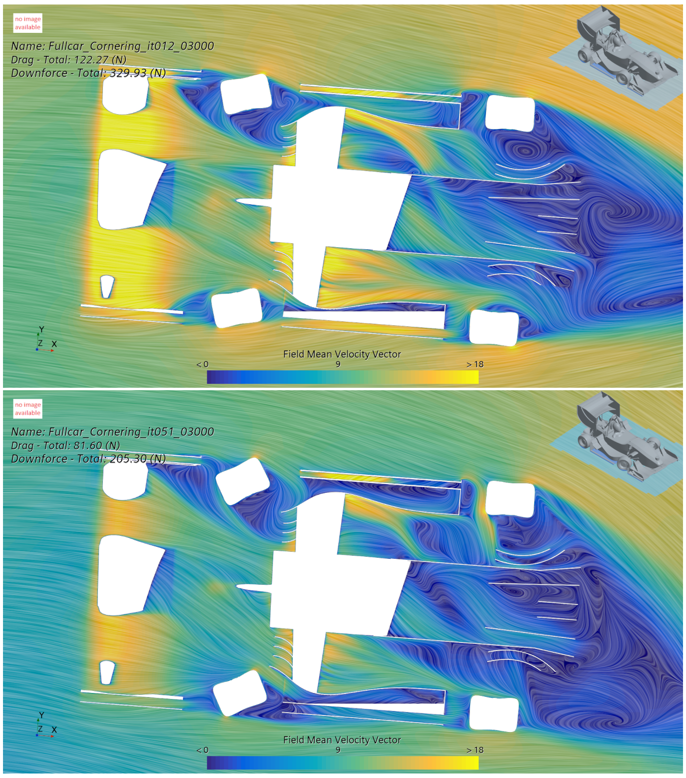

Figure 2.8: Flow separation in a Skidpad corner (top) and in a sharper corner (bottom).

It is visible how the dark blue areas, which denote separated regions, assume different shapes and get more intense in the right picture as the curvature of the airflow increases. This is a good example of how the drag generated by an aerodynamic package can vary as airflow follows a different path.

2.5.0.3 Ground Effect

Ground effect is the name given to an effective way of using the airflow under a car in order to generate downforce. This phenomenon, based on Bernoulli's principle, is characterized by the acceleration of air below the car and its expansion behind it, commonly done through diffusers.

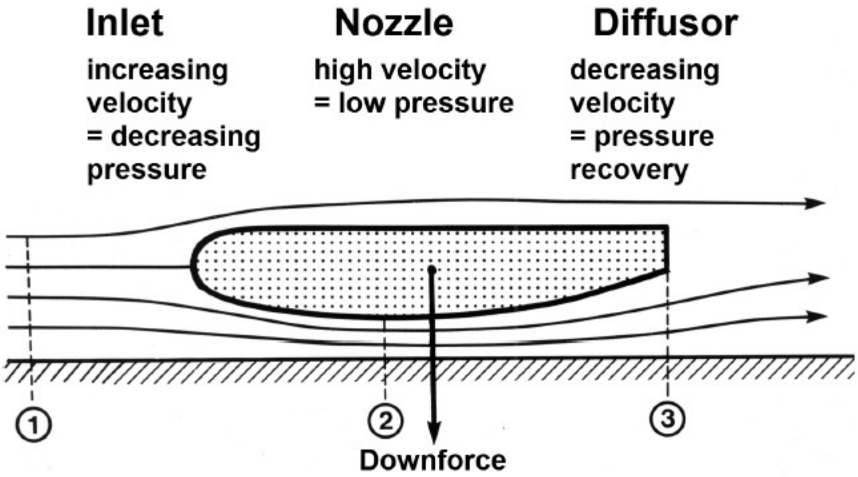

Figure 2.9: Ground effect mechanism. [9]

Its key parameter is ground clearance, which needs to be within a certain range for ground effect to be effectively generated. In case of an excessively reduced ground clearance the airflow would be choked, while a too large ground clearance would result in insufficient airflow acceleration; both cases would lead to a downforce loss.

During a corner the inner side of the car lifts while the outer gets pushed down. This causes ground clearance to increase on the inner side and decrease on the outer side, leading to potential losses on one or even both sides.

2.6 Interaction between Aerodynamics and Vehicle Dynamics

The use of aerodynamic devices leads to generation of downforce and therefore to the presence of another term influencing tire loads.

The impact that this has on the lateral and longitudinal dynamics of a race car is discussed in Sections 2.6.1 and 2.6.2, while Section 2.6.3 features a brief discussion about acceleration and braking scenarios.

2.6.1 Lateral Downforce Distribution

Figure 2.10 shows the same scenario as in Figure 2.1, where now DF and F_y are the downforce and side force generated by the vehicle due to its aero package, respectively.
F_{lz} indicates the normal loads acting on both the front and rear left tires as a whole, and F_{rz} does the same for the right tires.

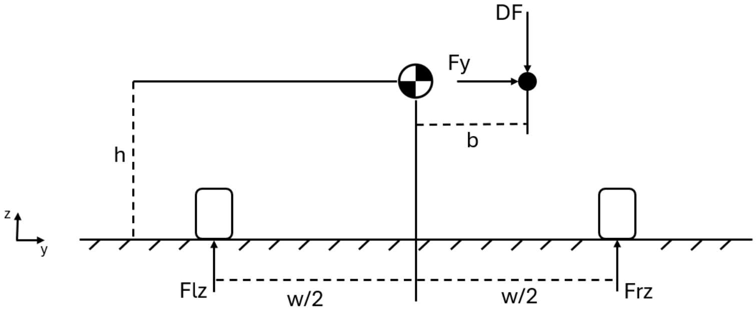

Figure 2.10: Free body diagram showing the lateral aerodynamics contribution to tire loads.

Downforce and side force (and drag, relevant in the next section) act on a point defined as the Center of Pressure (CoP) of the car, located at a generic lateral distance b from the CoG due to cornering dynamics, and assumed at a constant vertical distance h from the ground.
The aerodynamic contribution to the normal load acting on the left and right tires can be calculated as:

$$F_{lz} = \frac{\left(\frac{w}{2} - b\right) * DF - h * F_y}{w} \tag{2.16}$$

$$F_{rz} = 1 - F_{lz} \tag{2.17}$$

A parameter called Left Downforce Distribution (LDD) defined as the percentage of total downforce acting on the left tire can be obtained as:

$$LDD = 100 * \frac{F_{lz}}{F_{lz} + F_{rz}} \tag{2.18}$$

As for the intent of this project, managing to increase the value of LDD by acting on the aerodynamic package would ideally counteract the Lateral Load Transfer shift to the right intrinsecally caused by a left turn, thus improving the car's performance in cornering.

2.6.2 Longitudinal Downforce Distribution

Understeering and oversteering can be counteracted by changing where aerodynamic loads act, done by designing an aerodynamic package that generates more downforce closer to the front or the rear of the car, depending on specific needs.

Figure 2.11 shows a scenario where a race car is moving in the x-direction, where F_{fz} indicates the vertical load acting on the front axle and F_{rz} does the same for the rear axle; L is the car's wheelbase, defined as the distance between front and rear axles.

Aerodynamic downforce, DF, and drag, F_x, are considered to be applied in the CoP, which is placed at a certain vertical distance h from the ground and horizontal distance a from the rear axle; CoG is shown for reference, but it is not considered in the following calculations.

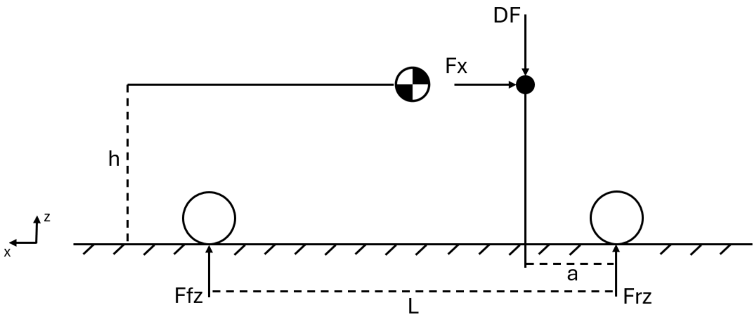

Figure 2.11: Free body diagram showing the longitudinal aerodynamics contribution to tire loads.

The aerodynamic contribution to the normal load acting on the front and rear axles can be calculated as:

$$F_{fz} = \frac{a * DF - h * F_x}{L} \tag{2.19}$$

$$F_{rz} = 1 - F_{fz} \tag{2.20}$$

A parameter called Front Downforce Distribution (FDD) defined as the percentage of total downforce acting on the front axle can be obtained as:

$$FDD = 100 * \frac{F_{fz}}{F_{fz} + F_{rz}} \tag{2.21}$$

When the value of FDD gets higher than 50% more downforce acts on the front axle, and contrary to CoG, this induces oversteer; when it is lower than 50% downforce is more concentrated on the rear axle, inducing understeer instead.
Therefore, it is important to distribute downforce properly to be able to counteract unwanted behaviors due to the front-rear CoG balance, also referred to as Weight Distribution (WD).

CFS' Suspension department designs for a WD balance of 49.5-50.5 %, meaning that the rear axle is more loaded and a slight oversteer is induced.
The aerodynamics team therefore designs for a FDD slightly lower than 50 %, between 47 and 49 %, to provide stability to the vehicle.

2.6.3 Acceleration and braking scenarios

Aerodynamic forces also have an impact on the car's behavior during acceleration and braking scenarios.

When accelerating, FDD tends to shift rearwards resulting in more load and grip to the rear tires enhancing the accelerating capabilities of the vehicle; similarly, in braking scenarios the value of FDD increases, shifting forward and making it easier to brake.

An optimized aerodynamic package is therefore crucial in order to design a car that can handle acceleration, braking and cornering scenarios properly.

2.7 CFD Theory

The first step of a solving process in CFD is the discretization of partial differential equations and generation of the mesh, which in Star-CCM+ is done through the Finite Volume Method (FVM).
In this section, however, focus will be on Turbulence Models only.

2.7.1 RANS - Reynolds Averaged Navier Stokes Equations

The RANS equations are time-averaged equations based on Reynolds decomposition of the equations of motion for fluid flows: they are used to describe turbulent flows through approximate time-averaged solutions to the Navier-Stokes equations.
For incompressible Newtonian fluids in stationary conditions, RANS can be written as

$$\rho \bar{u}_j \frac{\partial \bar{u}_i}{\partial x_j} = \rho \bar{f}_i + \frac{\partial}{\partial x_j}\left[-\bar{p}\delta_{ij} + \mu\left(\frac{\partial \bar{u}_i}{\partial x_j} + \frac{\partial \bar{u}_j}{\partial x_i}\right) - \rho\overline{u_i' u_j'}\right] \tag{2.22}$$

2.7.2 Turbulence Models

Turbulence models are tools used in CFD to efficiently approximate the behavior of complex turbulent flows.
Although different types of models exist, only RANS models are presented in this section, as these are the ones used by CFS and in this project.

2.7.2.1 $k - \epsilon$ Turbulence Model

The $k - \epsilon$ model is a RANS turbulence model based on the solution of two partial differential transport equations, where the variables are k, turbulence kinetic energy, and ϵ, rate of dissipation of k.
This is a simple model, good for handling complex geometries and fully turbulent, high-Re flows, but it is inaccurate with curved and low-Re flows.

2.7.2.2 $k - \omega$ Turbulence Model

This is a RANS model where the two partial differential transport equations are solved for k, similarly to the $k - \epsilon$ model, and for ω, the specific rate of dissipation of k.
It is a less simple model compared to $k - \epsilon$ and it has larger convergence times, but it is good for treating boundary layer flows and handling flow separation.

2.7.2.3 SST $k - \omega$ Turbulence Model

This model is characterized by a better handling of turbulent shear stress transport - thus SST - achieved through the combination of $k - \omega$, good with near-wall flows, and $k - \epsilon$, better for free-stream flows.
The SST $k - \omega$ model is the model used in this project.

3

Methods

The development of this study required a proper 3D model of the CFS25 car, setup of a CFD environment, analysis of CFD simulations and, at last, VD calculations to assess the behavior of the system.
Descriptions of the different stages are presented in this chapter.

3.1 CAD Phase

The car model used is a simplified version of Svea, as modelled by the CFS25 team on the Siemens NX software, where only Aerodynamics, Chassis and Suspension assemblies were imported.

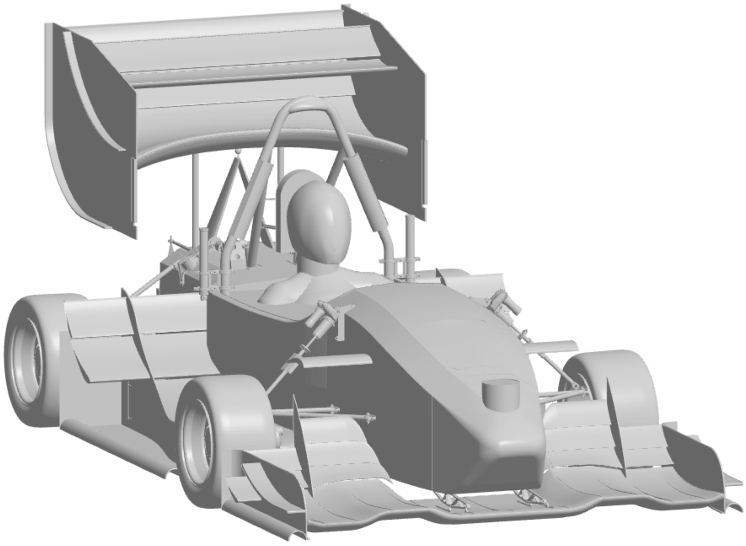

Figure 3.1: Model of Svea.

The Aerodynamics assembly does not include the cooling fans and radiators mounted on Svea's side wing endplates, with their slots being replaced by solid walls, and the Wheels Actuation assembly only features wheels, motors and the required linkages in order to properly simulate airflow blockage.

A cockpit closing cover similar to the one used by the team was modelled, to avoid meshing the interior of the monocoque, and the driver model was imported from the existing team's simulation files; the LiDAR, located on the Nose Cone, is a simple cylindric extrusion with the same dimensions as the one mounted on Svea.

The main difference between Svea and the model used is related to the rear wing mountings, that needed to be redesigned to allow the wing rotation similarly to the Centripetal Wing's actuation.
A simple triangular airfoil-shaped mounting solution, shown in Figure 3.2, was modelled, with a made-up ball joint just under the wing around which the device rotates; a simple pipe, resembling the dampers used by Zenvo, was placed at each side of the mounting.

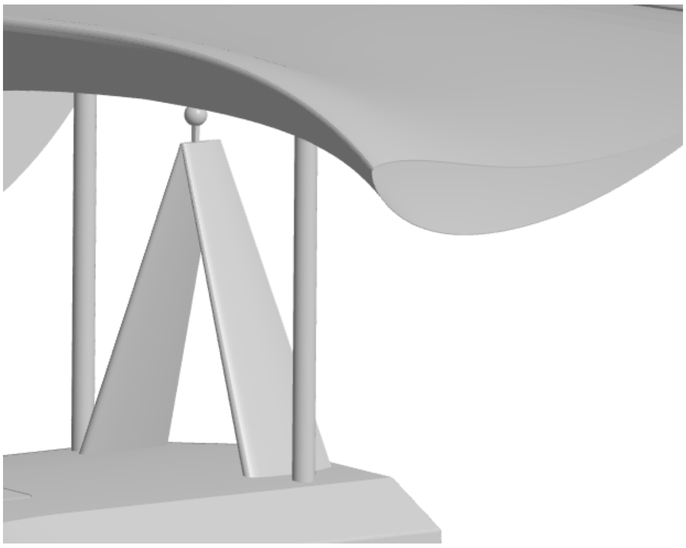

Figure 3.2: New RW mountings.

The whole structure was mounted on the rear of the monocoque, behind the head restraint and between the rear actuation, which is the only possible placement given the current car's design as can be seen is Figure 3.3.

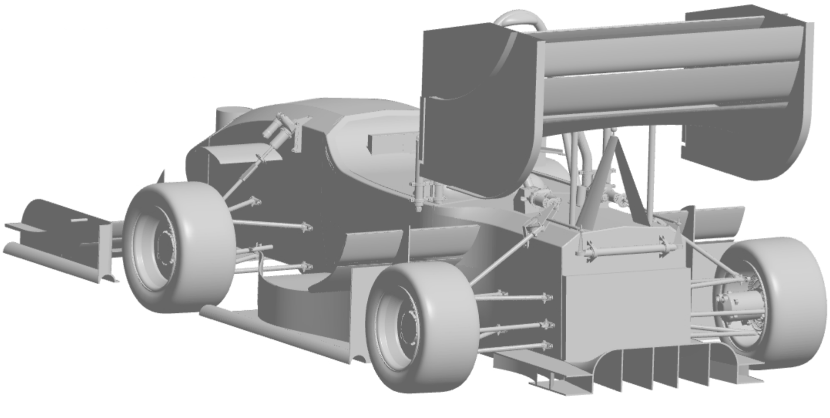

Figure 3.3: Rear view of Svea with RW Mounting placement visible.

3.2 CFD Phase

A new cornering simulation setup was created in Star-CCM+, both to carry out this project and to be handed over to CFS for the upcoming years.

3.2.1 Domain

In CFD, the scenario in which a car takes a corner is simulated using curved domains, where the air is forced to follow a curved path around the vehicle.
This required building a new Wind Tunnel model, which was done following a study published by Siemens in collaboration with Queen's Formula SAE. [11]
The intensive use of parameters allowed to use the same Wind Tunnel geometry for all the different cases, with minor modifications needed in order to leave enough space around and over the car.

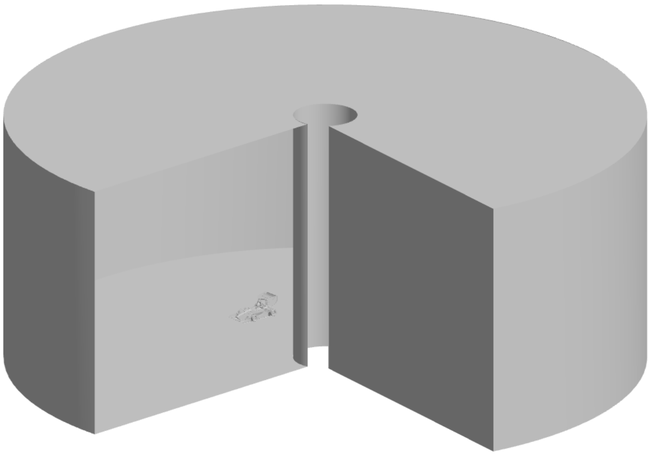

Figure 3.4: Wind Tunnel model with car position visible.

3.2.2 Physics Continuum models

The models used for the physics continuum are listed in Table 3.1

Table 3.1: Physics continuum models.

All y+ Wall Treatment	Segregated Flow
Cell Quality Remediation	Solution Interpolation
Constant Density	SST (Menter) K-Omega
Gas: Air	Steady
Gradients	Three Dimensional
$k-\omega$ Turbulence	Turbulent
Reynolds-Averaged Navier-Stokes	Wall Distance

3.2.3 Pre-processing operations

Six initial operations are performed before meshing, to get the car in the correct scenario.

To simulate the side slip of the car, the wind tunnel is first rotated around its center by a quantity equal to $-BodySlipAngle$.

The Rear Wing is rotated around the longitudinal axis of the car (around the ball joint) by the specific angle to be tested, then the whole sprung mass of the car is rotated around the longitudinal axis by a quantity equal to $RollAngle$, and the wheels are rotated around the vertical axis by a quantity equal to their respective $SteeringAngle$.

At last, the whole car model is translated downwards by 8 mm, to simulate contact patch deformation, with the car ending in the same position CFS designs for.

The values for body slip, roll and steering angles are taken from on-track testing and real competition data recorded on the CFS24 car, Freja, during the 2024 season, for the same cornering radii simulated in this project; the configuration in which the car model gets meshed is finally shown in Figure 3.5

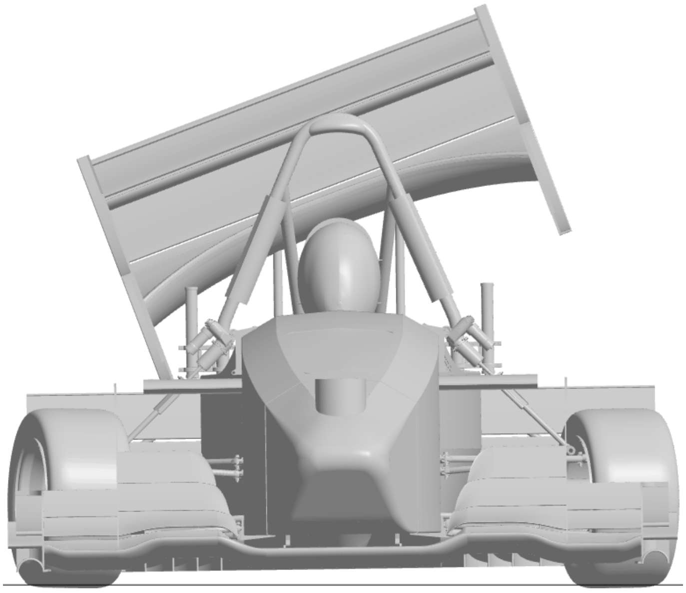

Figure 3.5: Car model after operations, for a 20°-tilt Skidpad scenario.

3.2.4 Mesh

The meshing operation consists of a surface wrapper over the car, its subtraction from the Wind Tunnel, and an Automated mesh at last.
Descriptions of these operations are given in this section.

3.2.4.1 Surface Wrapper

The first mesh operation is a surface wrapper over the surface of the car, with a base size of 20 mm; the custom controls listed in table 3.2 are applied over the curves and surfaces of the Aerodynamics and Chassis assemblies to better control the quality of the mesh.

Table 3.2: List of surface wrapper refinements.

Assembly	**Target Surface Size [%]**	**Minimum Surface Size [%]**
Front Wing	4.5	2
Rear Wing	7.5	2
Side Wings	7.5	2
Diffuser	7.5	2
Chassis	7.5	2

3.2.4.2 Automated Mesh

After the subtract operation, and automated mesh is performed on both Wind Tunnel and car with trimmed cells, 5 prism layers and a base size of 20 mm.

Here, an additional surface control is applied on the Wind Tunnel: inlet, outlet and floor have a target surface size of 100 mm, to properly approximate the airflow without getting a too fine mesh, while for ceiling and the lateral walls it is set at 600 mm as gradients are not expected on those surfaces and a fine mesh is unnecessary.

Volumetric refinements are applied on the floor, around the wheels, at the near, mid and far rear wake and around the whole car, to better approximate wake and airflow in crucial regions.

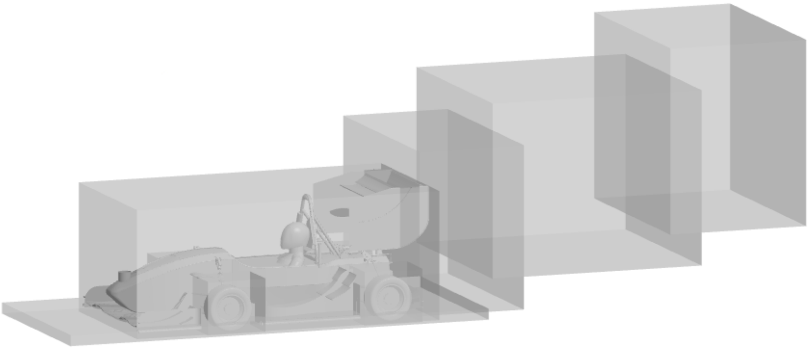

Figure 3.6: Volumetric refinements, from left to right: Floor, Main, Wheels, Near Wake, Mid Wake, Far Wake.

Table 3.3: List of volumetric refinements.

Volume	**Custom Size [%]**
Main	70
Floor	80
Wheels	70
Near Wake	70
Mid Wake	75
Far Wake	80

3.2.5 Boundary Conditions

Boundary conditions are taken from the current CFS cornering setup, set as if the car was fixed and the air flowed around it; they are listed in Table 3.4.

Table 3.4: Boundary conditions used in the CFD simfile.

Region	**Condition**	**Value**
Wind tunnel inlet	Velocity inlet	[0,0,0] km/h
Wind tunnel outlet	Pressure outlet	0 Pa
Wind tunnel floor	Moving wall	[0,0,0] km/h
Wind tunnel ceiling, walls	Symmetry plane	-
Wheels	Rotating wall	54.3 rad/s
Rest of car	Wall	0 km/h

The reason why inlet and floor have a null velocity is that they are contained in a rotating reference frame that is moving around the vertical axis, so a velocity equal to v_c is already assigned there; v_c is defined as

$$v_c = \frac{FreeFlowVelocity}{CorneringRadius} \tag{3.1}$$

The wheels velocity is set using the following formula:

$$WheelVelocity = 2 * \frac{FreeFlowVelocity}{WheelDiameter} \tag{3.2}$$

Therefore it automatically changes when the $FreeFlowVelocity$ parameter changes, depending on the simulated scenario.

A more vehicle dynamics-focused project might improve this by setting for each wheel their respective velocity, but given the limited difference in percentage that would make, this formula allows to simplify calculations while still keeping a good correlation to reality.

3.2.6 Simulations

Trying to simulate an unsteady flow using steady state equations generates oscillations in the results coming from every iteration, therefore a certain number of iterations is performed until values closely oscillate around the same value: similarly to what is done by CFS, in this project 3000 iterations are performed and then average values for each coefficient from the last 500 iterations are saved.

3.2.6.1 Scenarios

The changes in parameters performed in every simulated scenario are listed in Table 3.5.

Table 3.5: Settings for simulated scenarios.

Scenario	Sharp corner	Skidpad corner	Wide corner
Cornering Radius [m]	4.5	8.5	18
Free Flow Velocity [km/h]	30	40	62
Body Slip Angle [°]	3	1.8	4.5
Roll Angle [°]	0.75	0.8	0.9
Inner Wheel Steering Angle [°]	26.7	14.4	6.4
Outer Wheel Steering Angle [°]	29.7	15.1	6.5

For each cornering scenario the Rear Wing is tested in different tilted configurations, from 0° up to 20°, to get trends for all relevant attributes.

3.2.7 Post-Processing

Every simulation is post-processed, leading to the production of data and images for numerical and visual analysis, respectively.

Field functions, reports, plots and monitors needed for the collection of forces and force coefficients were initially imported from the team's simulation files, but new reports and modifications of the imported ones were required to adapt all formulas to the new simulation environment; in particular, the creation of a new report was necessary in order to calculate the Lateral Load Transfer shift.

Section views are produced at regular steps for all three planes, allowing to produce mesh, pressure coefficient, skin friction, velocity vector and vorticity vector pictures used for visual analysis.

Modified versions of the Star-CCM+ Macro and MATLAB scripts developed by CFS were used in this phase, for running the post-processing macro on Star-CCM+ and extracting the final averaged data, respectively.

3.3 Vehicle Dynamics Phase

VD calculations represent the last stage of the workflow and are based on models and data given by the Vehicle Dynamics department of CFS25.

First, the normal loads on each tire are calculated with the following formulas:

$$F_{z_{FL}} = \frac{1}{2} * m * g * WD - \frac{m * \frac{v^2}{R} * h}{T} * LLTD + DF * FDD * LDD \tag{3.3}$$

$$F_{z_{FR}} = \frac{1}{2} * m * g * WD + \frac{m * \frac{v^2}{R} * h}{T} * LLTD + DF * FDD * (1 - LDD) \tag{3.4}$$

$$F_{z_{RL}} = \frac{1}{2} * m * g * WD - \frac{m * \frac{v^2}{R} * h}{T} * LLTD + DF * (1 - FDD) * LDD \tag{3.5}$$

$$F_{z_{RR}} = \frac{1}{2} * m * g * WD + \frac{m * \frac{v^2}{R} * h}{T} * LLTD + DF * (1 - FDD) * (1 - LDD) \tag{3.6}$$

where:

- FL, FR, RL and RR indicate the Front Left, Front Right, Rear Left and Rear Right tire;
- m is the sum of the car's mass, 205 kg according to CFS25 team goals, and driver's mass, set at 70 kg, for a total of 275 kg;
- g is the gravitational acceleration, set as 9.81 m/s^2;
- v is the Free Flow Velocity, to be changed according to the simulated scenario;
- R is the Cornering Radius, to be changed according to the simulated scenario;
- h is the vertical distance of Svea's CoG from the ground, set at 0.275 m according to CFS25 design;
- T is Svea's track width, set at 1.25 m according to CFS25 design;
- $LLTD$, Lateral Load Transfer Distribution, is the percentage of LLT concentrated on the front axle, assumed equal to WD and therefore set at 49.5 %.

The tire model in Figure 2.2 is used to calculate the lateral load generated by every tire; the four lateral forces are then summed up, assuming all forces to be applied in one point, allowing to calculate lateral acceleration, cornering speed and, ultimately, laptime with the following formulas:

$$a_y = \frac{\sum F_y}{m} \tag{3.7}$$

$$v = \sqrt{\frac{2\pi R}{a_y}} \tag{3.8}$$

$$t = \frac{2\pi R}{v} \tag{3.9}$$

Finally, graphs are produced in order to visualize trends and assess the validity of the system.

4

Results

The results for each scenario are reported in this chapter, together with discussions that aim to explain the extracted data.

Every section features results, given in the form of tables and graphs to properly illustrate trends and special cases, and discussions needed in order to thoroughly investigate the reasons behind each behavior, for which post-processing pictures are used as aid.

4.1 Skidpad corner

For Skidpad, considered as the baseline scenario, results are given in this section.

4.1.1 Downforce

Downforce values for the whole car and the specific aerodynamic devices are listed in Table 4.1.

Table 4.1: Downforce values for the Skidpad cornering scenario.

Angle [°]	Total [N]	FW [N]	RW [N]	SW [N]	Diffuser [N]
0	329.9	127.2	85.3	87	45.2
2.5	328.8	125.1	89.8	87.6	41.1
5	325.3	127.8	83.9	87.5	40.8
7.5	328.4	126.2	79.5	92.2	45.2
10	327.5	122.5	78.1	94.8	47
12.5	326.6	125.6	74.5	95	46.5
15	328.2	126.8	71.8	96.2	48.2
17.5	325.1	121.4	71.7	97.8	49.2
20	318	121.3	69	94.5	48.1

With the aid of the pictures below it can be observed that the total downforce generated in this configuration tends to decrease as the RW gets tilted, although two deviations from the overall trend are visible at 5° and 15°, while the specific parts show different behaviors; it has to be kept in mind that these graphs only show data for a limited number of setups, therefore running simulations on intermediate tilt configurations might show true local minimums and maximums somewhere else.

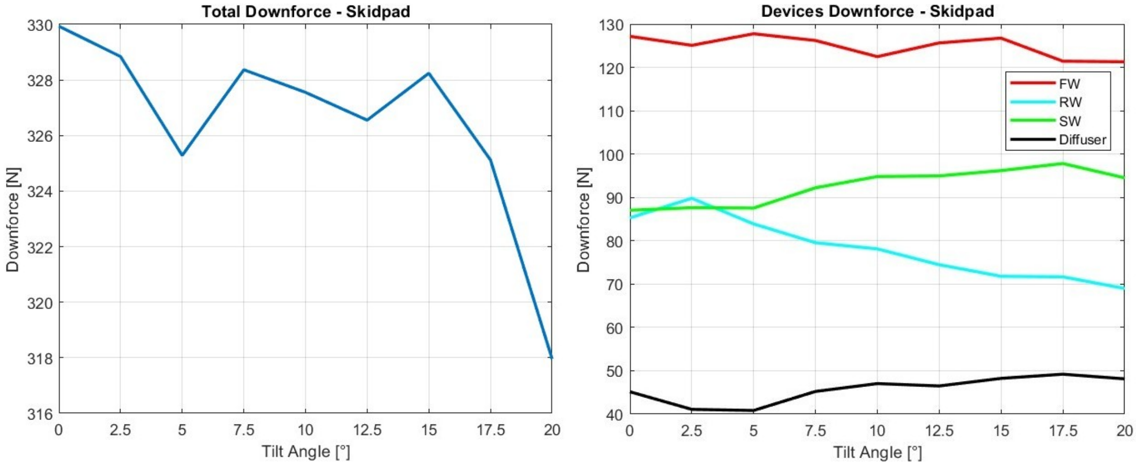

Figure 4.1: Downforce values for the Skidpad cornering scenario.

In particular the downforce generated by the RW decreases, meeting theoretical expectations, except for a maximum at the 2.5° tilt where it generates 5.3 % more downforce compared to the no-tilt configuration.

Figure 4.2, captured right after the leading edge of the RW, shows a slightly faster airflow (intense yellow) under the tilted wing, mostly concentrated in the central region, which could explain the local downforce increase.

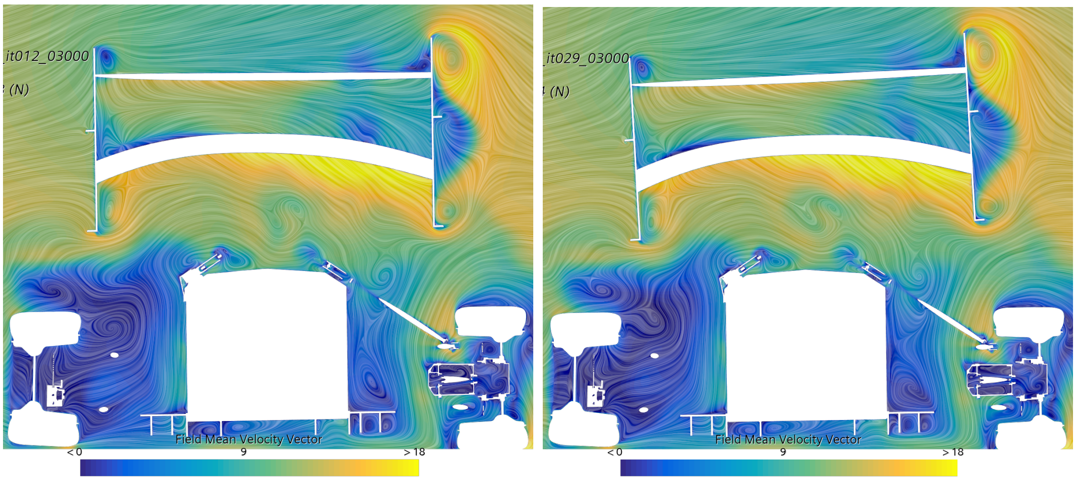

Figure 4.2: Flow velocity vector pictures for no-tilt (top) and 2.5°-tilt (bottom) configuration, frontal view, taken 2.5 m from the most forward point of the car.

The comparison between the no-tilt and maximum-tilt configurations is shown in Figure 4.3, taken 25 cm right of the car's centerline, where the influence that the RW and the rest of the car have on each other is easily noticeable.
When the right side of the wing is lowered (right picture) it gets close enough to the

monocoque and the SW, ending up working in a wake region: pressure under the wing increases and the downforce that it generates is lower.

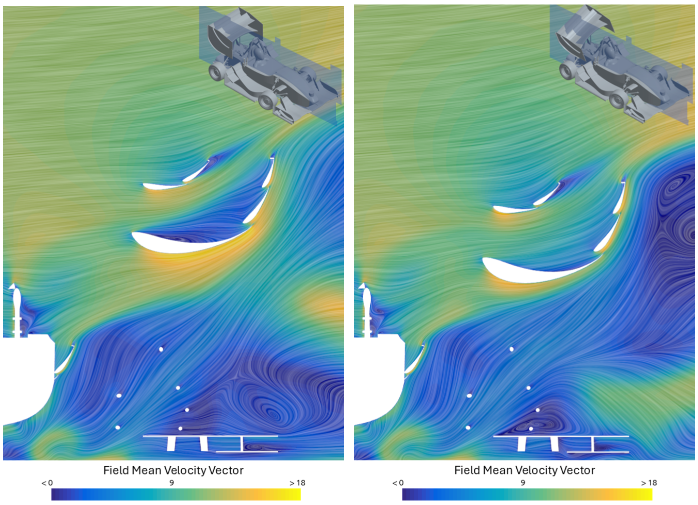

Figure 4.3: Flow velocity vector pictures for no-tilt (left) and 20°-tilt (right) configuration, lateral view, taken 15 cm right of the centerline of the car.

Figure 4.4 can instead be used to compare the left side of the RW, that gets lifted in the 20°-tilt configuration shown on the right. The low pressure region under the wing gets larger when the wing is lifted and less influenced by what is in front; the gain coming from this side is anyway smaller than the loss occurring on the right side, ultimately resulting in a 19% RW downforce loss.

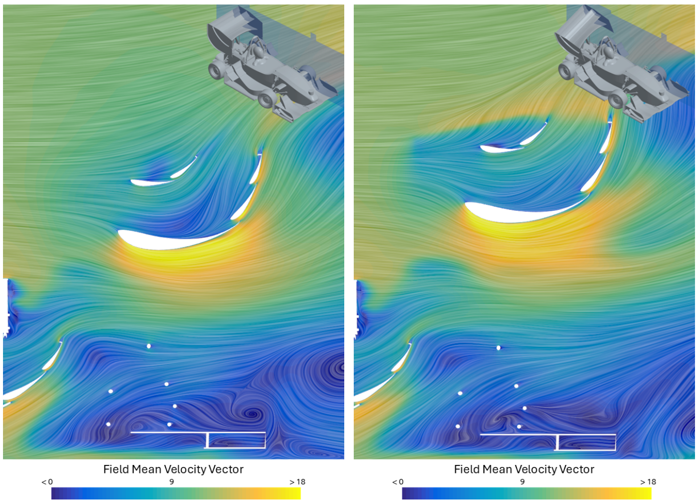

Figure 4.4: Flow velocity vector pictures for no-tilt (left) and 20°-tilt (right) configuration, lateral view, taken 22 cm left of the centerline of the car.

The downforce generated by the diffuser sees a minimum when the RW is tilted by 5°, resulting in a 9% loss; it then increases again up to 17.5° for a maximum 9% gain over the baseline, before settling down at a final 6.6% gain for the 20° case.

The flow pictures in Figure 4.5 below show how the rear low wake region changes in shape due to the different configuration of the RW. It appears that the wake coming from the rear right tire and the diffuser gets directed towards the inner side of the car where the vertical distance between RW and diffuser gets larger.

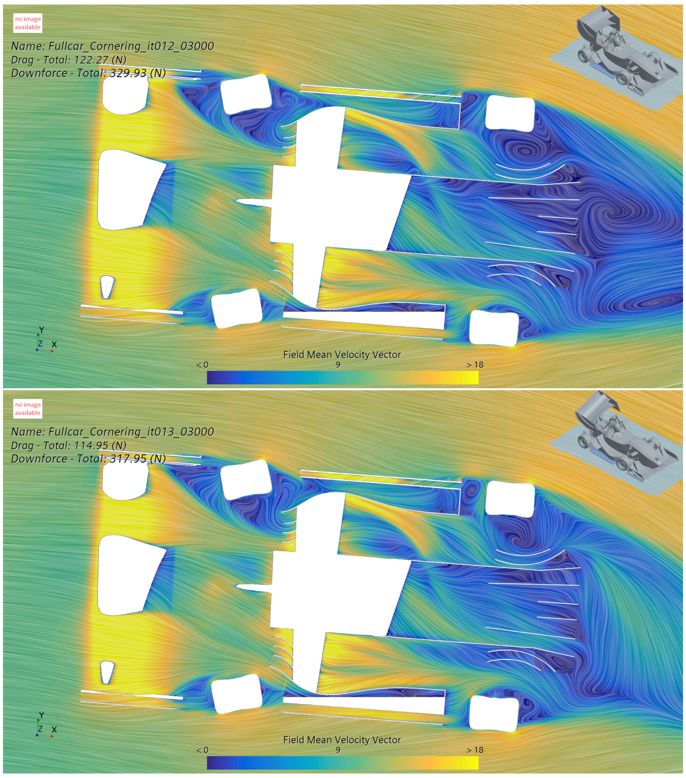

Figure 4.5: Flow velocity vector pictures for no-tilt (top) and 20°-tilt (bottom) configuration, top view, taken 6 cm above the ground.

This inwash is most likely generated by the right RW endplate getting close to the monocoque, as visible in Figure 4.6.

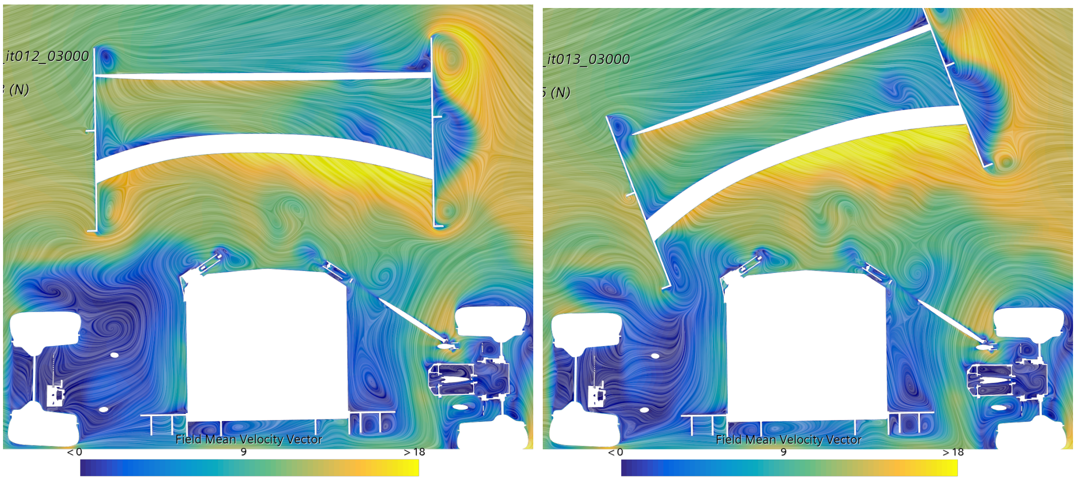

Figure 4.6: Flow velocity vector pictures for no-tilt (left) and 20°-tilt (right) configuration, frontal view, taken 2.5 m from the most forward point of the car.

The right tire wake appears to be disrupted by this interaction, leading to a the formation of a low pressure region between tire and endplate that extends to the left as shown in Figure 4.7.

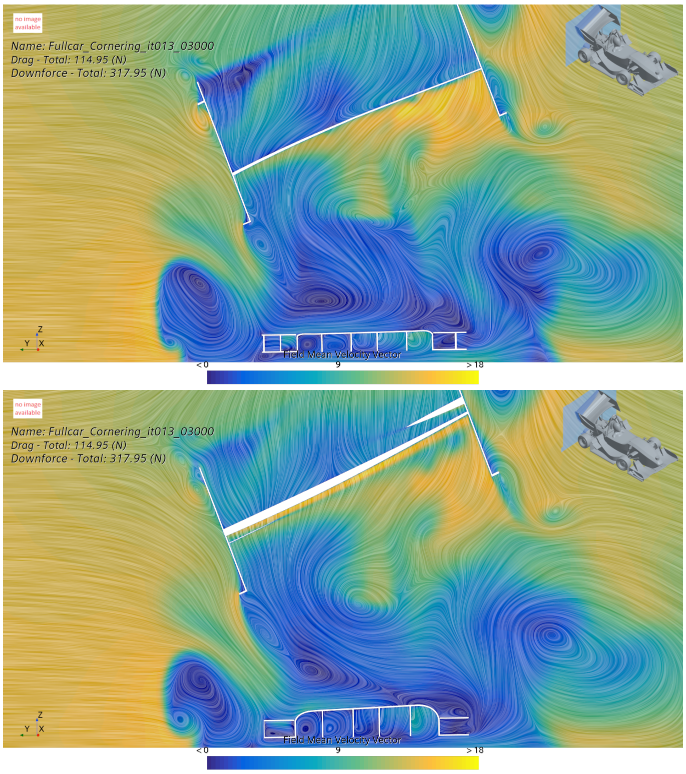

Figure 4.7: Inwash expansion in the 20-tilt configuration, frontal view, taken 2.8 m (top) and 2.9 m (bottom) from the most forward point of the car.

With a behavior similar to that of the diffuser, after staying mostly constant until the 5°-tilt, the SW assembly starts to generate more downforce and eventually reaches its peak at the 17.5°-tilt configuration. The maximum increase is 12.4% of its initial value, then it settles down at a final 8.5% gain.
Figure 4.5 also shows that the left SW, closer to the center of the corner, is the one generating most of the downforce; this is mostly due to the blockage that the front right tire creates in front of the right wing.
It can also be noted that the separation coming from the right FW endplate, much larger than that generated on the left side, reduces the amount of high-energy airflow under the right SW leading to the mentioned downforce imbalance to the left.

In terms of pure numbers, the FW is the device with the most oscillatory downforce behavior, despite a general decreasing trend; the largest loss (4%) occurs at the largest RW tilt. The mentioned wake region generated by the right endplate changes the extraction of air from the underbody, resulting in most of the downforce being generated by the left side.

As mentioned at the beginning of this section, the total downforce trend shows a general decrease at every increase of the RW tilt angle.
This meets the expectations coming from Zenvo's data: the maximum overall loss

caused by tilting Svea's RW by 20° would result in a 3.6% loss, just slightly larger than the 3% experienced on the TSR-S.

The trend is, however, irregular and presents two anomalies, with a local minimum at 5° and a local maximum at 15°, following the trends of the different devices: the small loss at 5° occurs where the diffuser loss is the main difference compared to the baseline case, and the small gain at 15° happens when FW, SW and diffuser are almost at their maximum peak.

4.1.2 Downforce distribution and tire loads

The results for the front and left downforce distribution and the normal and lateral tire loads are given in tables 4.2 and 4.3; FDD and LDD are presented in both tables for easier reference.

Table 4.2: Downforce distribution and normal tire load values for the Skidpad cornering scenario.

Angle [°]	**FDD [%]**	**LDD [%]**	$F_{Z_{FL}}$ [N]	$F_{Z_{FR}}$ [N]	$F_{Z_{RL}}$ [N]	$F_{Z_{RR}}$ [N]
0	58	61.7	350.7	1176	322.9	1178.1
2.5	56.3	62.6	348.8	1171.9	327.3	1178.6
5	58.8	63.3	353.7	1172.9	322.2	1174.2
7.5	59.6	63.6	357.1	1173.9	321.8	1173.3
10	58.8	64.7	357.4	1170.6	324.8	1172.5
12.5	60.8	64.8	361.4	1172.4	320.5	1170
15	61.4	65.1	363.9	1172.9	320	1169.2
17.5	59.9	66.1	361.4	1168.7	323.6	1169.1
20	60.8	66.9	362.1	1166.5	320.9	1166.2

Table 4.3: Downforce distribution and lateral tire load values for the Skidpad cornering scenario.

Angle [°]	**FDD [%]**	**LDD [%]**	$F_{Y_{FL}}$ [N]	$F_{Y_{FR}}$ [N]	$F_{Y_{RL}}$ [N]	$F_{Y_{RR}}$ [N]
0	58	61.7	586.1	1663.6	542.5	1665.8
2.5	56.3	62.6	583.1	1659.3	549.4	1666.3
5	58.8	63.3	590.8	1660.4	541.3	1661.7
7.5	59.6	63.6	596.1	1661.4	540.8	1660.8
10	58.8	64.7	596.6	1657.9	545.4	1660
12.5	60.8	64.8	602.8	1659.9	538.6	1657.3
15	61.4	65.1	606.7	1660.4	537.9	1656.5
17.5	59.9	66.1	602.8	1656	543.5	1656.4
20	60.8	66.9	603.9	1653.7	539.3	1653.3

Due to the almost linear loss of RW downforce and the fact that FW and SW have generally oscillating or increasing trends, FDD slightly increases meaning that the balance shifts forward, with some oscillations due to specific cases already seen in the previous section.

Meeting expectations, the LDD value increases meaning that the overall normal load shifts towards the inner side of the car as the RW is tilted; unlike FDD, this happens with a reasonably regular trend and agrees with the fact that the left side of the Rear Wing is the one generating most of the rear wing downforce.
The 5% lateral shift is much lower than the 30% found by Zenvo, which is most likely due to the rear wing producing of the downforce on the TSR-S.

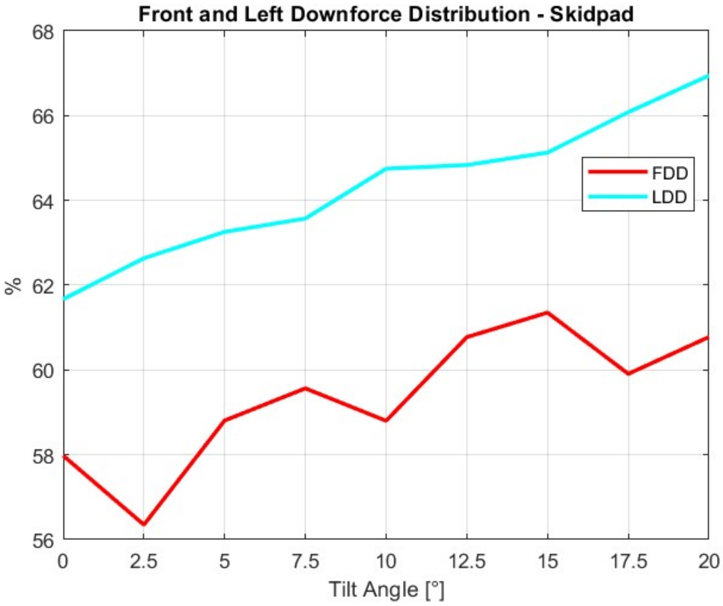

Figure 4.8: FDD and LDD trends for the Skidpad cornering scenario.

Figure 4.9 presents the trends for normal tire loads, with the left tires on the left and the right tires on the right.

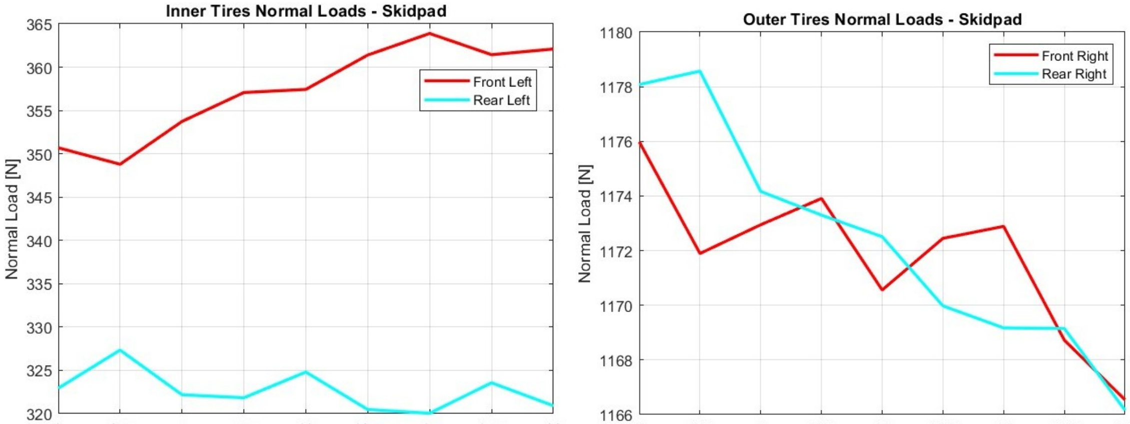

Figure 4.9: Normal tire load trends for the Skidpad cornering scenario.

All trends agree with the results coming from downforce and downforce distributions.

The front left tire is the only one gaining load, due to the balance generally moving both left and forward; the rear left has an oscillatory behavior, mostly depending on FDD oscillations and meaning that it might be more susceptible to longitudinal rather than lateral balance shifts.
Both outer tires lose vertical load overall, with the front right presenting a highly oscillatory trend: this tire is clearly influenced by FDD and the FW behavior, as the local minimums of $F_{Z_{FR}}$ and FW DF coincide. The normal load on the rear right tire follows a monotonous trend, and it slightly increases at the 2.5°-tilt configuration where the balance shifts backwards more than to the left.

The trends for lateral tire loads are presented in Figure 4.10.

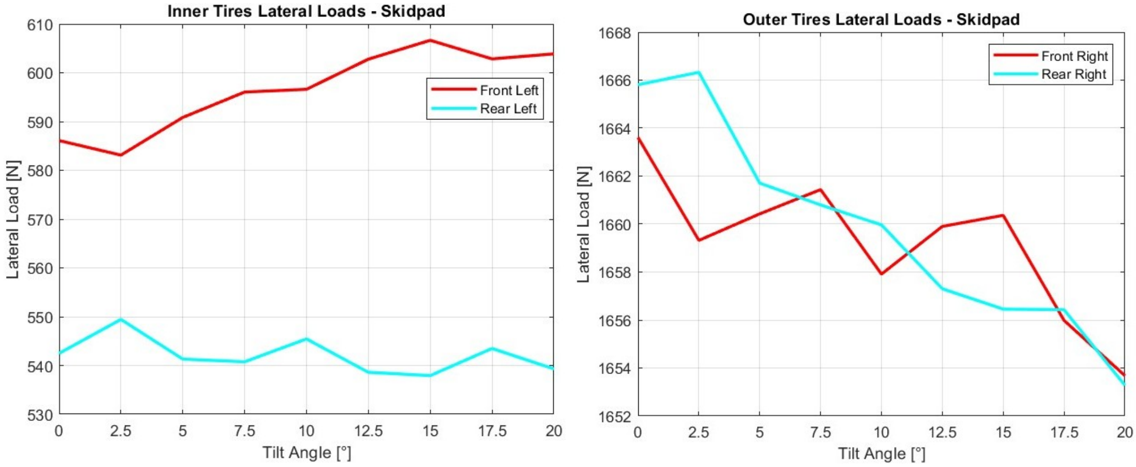

Figure 4.10: Normal tire load trends for the Skidpad cornering scenario.

It can be noted that the lateral loads generated by each tire follow the same trend as the normal load.
For the inner tires, the same percentage of variations occurs between normal and lateral loads for consecutive RW configurations, and since lateral loads are larger in magnitude, variations are slightly larger in absolute numbers.
For the outer tires what stays the same is the magnitude of variation, meaning that the same decrease or increase in N happens for both graphs at every consecutive configuration.

4.1.3 Laptimes

The results for the Skidpad laptimes are given in Table 4.4, and Figure 4.11 shows that they are closely linked to the total downforce generated at each configuration, with an overall inverse trend compared to downforce.
It is important to note, however, that the largest laptime gain is obtained at the 15°-tilt configuration, when total downforce only reaches its fourth maximum peak; at the same time the downforce distribution plots show that this is the most forward

load balance scenario, where the FL tire produces its maximum lateral load and the FR tire is at its third highest.

Table 4.4: Laptimes for the Skidpad cornering scenario.

Angle [°]	Laptime [s]
0	4.5497
2.5	4.5496
5	4.5516
7.5	4.5492
10	4.5487
12.5	4.5494
15	4.548
17.5	4.5494
20	4.5538

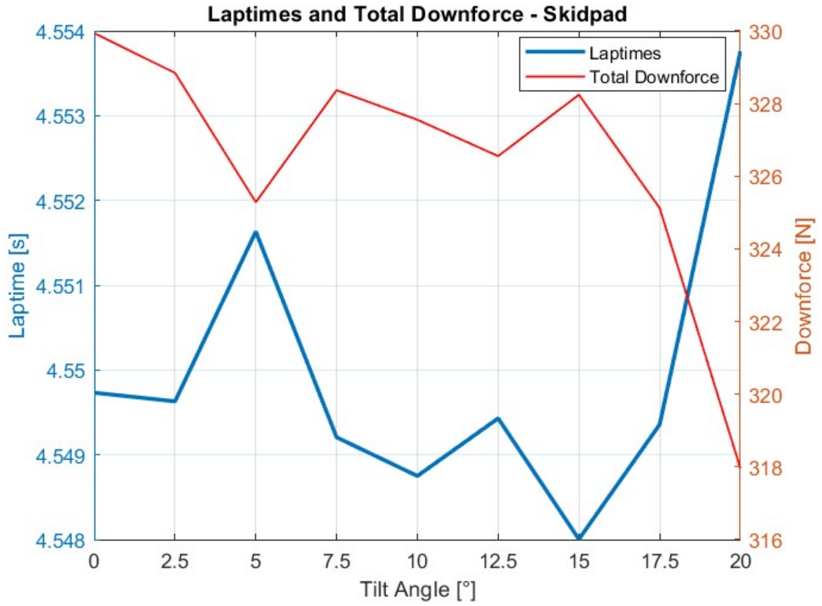

Figure 4.11: Laptime and total downforce trends for the Skidpad cornering scenario.

This shows the influence that balance and tire loads have on laptimes, even if the resulting gain is only 1.7 ms in this case.

4.2 Sharp corner

The results for the sharp corner are presented in this section.

4.2.1 Downforce

Downforce values for the whole car and the specific aerodynamic devices are shown in Table 4.5.

Table 4.5: Downforce values for the Sharp corner scenario.

Angle [°]	Total [N]	FW [N]	RW [N]	SW [N]	Diffuser [N]
0	205.3	62.4	56.6	68.4	28.4
2.5	204.4	62.9	53.2	69.9	29.2
5	198.9	61.4	49.8	69.2	29.4
7.5	190.2	60.9	46.5	64.9	28.4
10	186.9	60.6	44.4	64.5	28.1
12.5	182.1	60.6	44.4	62.1	25
15	177.2	59.7	39.4	61.2	26.8
17.5	180.2	61.2	41.1	62.3	25.9
20	173.3	60.6	37.7	59.2	25.9

The total downforce generated, as visible in Figure 4.12, tends to decrease as the RW gets tilted, except for a local maximum at the 17.5°-tilt configuration. This trend meets Zenvo's findings only in shape but not in overall values, since it results in a 15.6% loss, 5 times larger than the 3% measured on the TSR-S and 4.5 times larger than the result of the Skidpad scenario. This coincides with a small RW and SW downforce increase in the same case, while FW and diffuser balance each other.

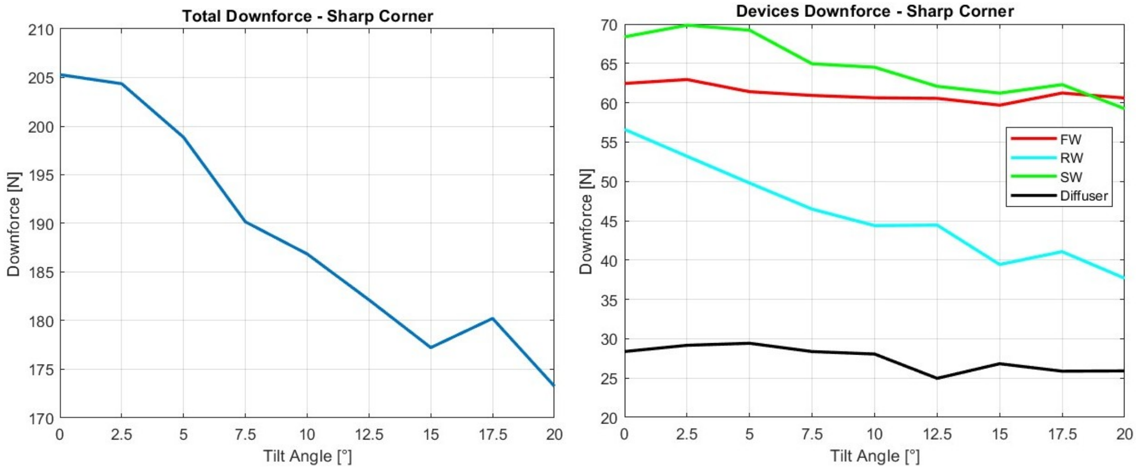

Figure 4.12: Downforce trends for the Sharp corner scenario.

The RW downforce trend shows a generally regular decrease all the way to 20°, meeting theoretical expectations, except for the already mentioned local maximum at the 17.5°-tilt configuration.

Figure 4.13 shows the right side of the wing in the no-tilt and maximum-tilt configurations, where it is easy to notice a formation of eddies behind the wing, most likely caused by the large tilt angle.

This is also supported by Figure 4.14 that, together with a generally lower flow velocity under the wing, shows that the right side gets too close to the rest of the car producing only a small portion of its initial downforce.

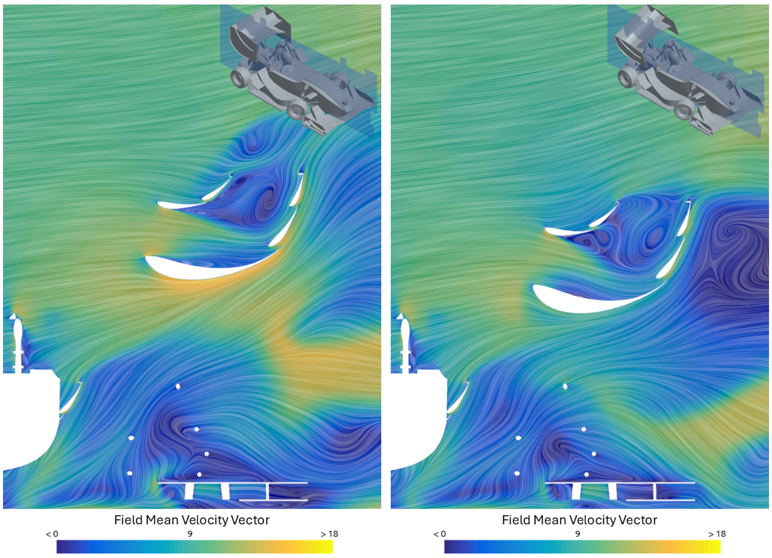

Figure 4.13: Flow velocity vector pictures for no-tilt (left) and 20°-tilt (right) configuration, lateral view, taken 15 cm right of the centerline of the car.

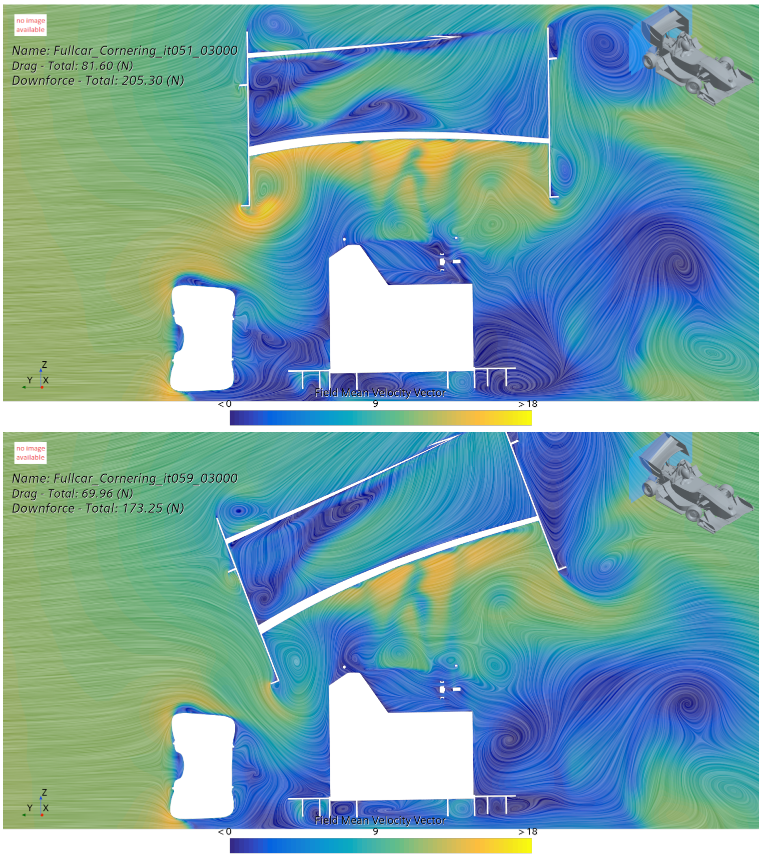

Figure 4.14: Flow velocity vector pictures for no-tilt (top) and 20°-tilt (bottom) configuration, frontal view, taken 2.7 m from the most forward point of the car.

The total downforce loss for the RW is again expectedly recorded at the maximum tilt, with a 33.3% loss that is way larger than the 19% measured in the Skidpad scenario.

Differently from the previous findings, the behavior of the SW downforce in the Sharp corner scenario sees, after an initial 2% increase, a continuous drop until a final 13.3% decrease when the RW is fully tilted. The only visible difference between the initial and fully tilted configurations is given in Figure 4.15, featuring a comparison between the different airflow extraction from the right SW top flap in the two cases.

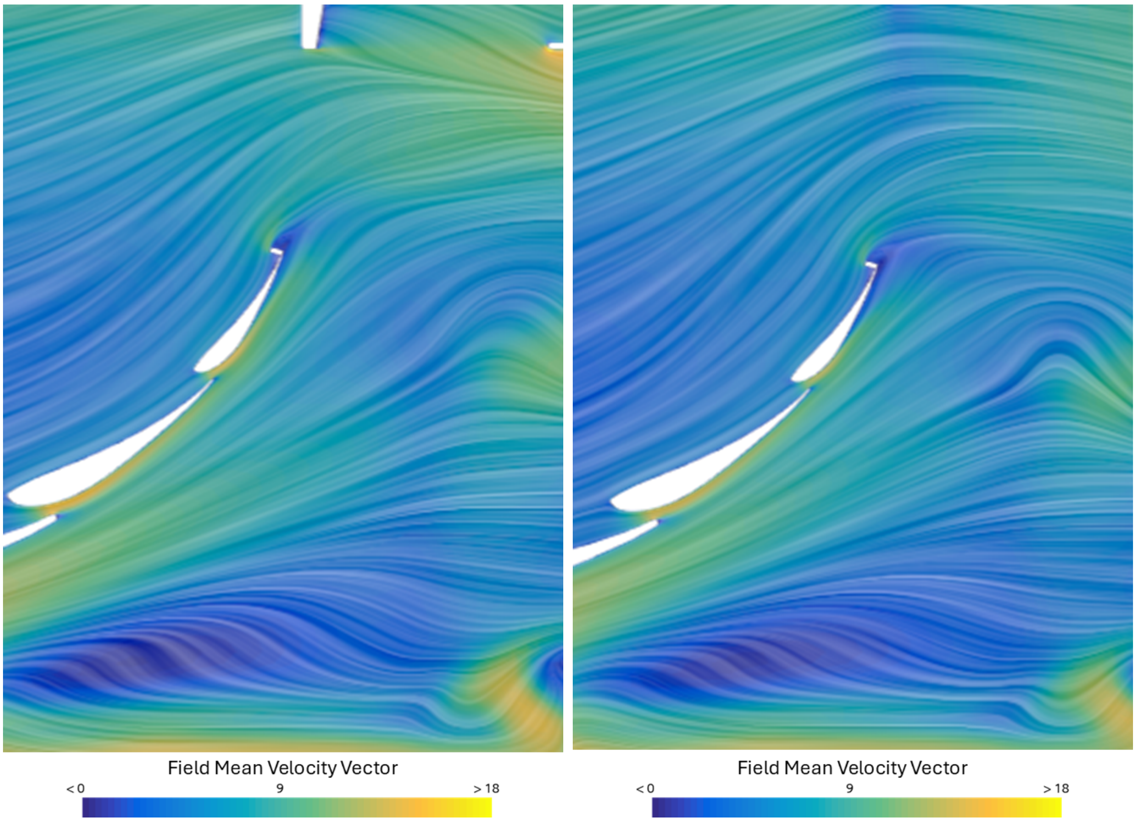

Figure 4.15: Flow velocity vector pictures for no-tilt (left) and 20°-tilt (right) configuration, lateral view, taken 28 cm right of the centerline of the car.

What appears is that the smaller distance between SW and RW changes how air is extracted from the top flap making it separate more, as can be noticed from the larger blue region around the suction side.

Figure 4.16 below shows that the flow through the underbody does not change much in the two cases at least regarding the SW, while the rear is again more affected.

From the pictures it is again visible a change of flow velocity and direction in the low rear wake region due to the influence of the RW.
The flow gets accelerated and directed towards the center of the corner, similarly to what was observed in the Skidpad scenario.

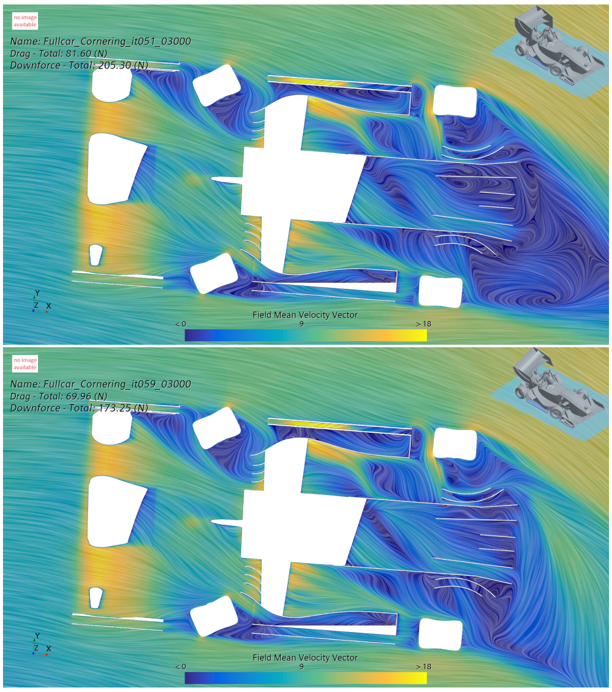

Figure 4.16: Flow velocity vector pictures for no-tilt (top) and 20°-tilt (bottom) configuration, top view, taken 6 cm above the ground.

The downforce generated by the diffuser stays overall constant, oscillating around the initial value. The FW presents a mostly constant behavior, with the largest downforce loss being only 4.4%, before a final slight increase for a final loss of just 3%. Figure 4.16 can also be used to see that the flow under the wing is more unbalanced to the left compared to the Skidpad scenario, again due to the wake generated by the right endplate.

4.2.2 Downforce distribution and tire loads

The results for the front and left downforce distribution and the normal and lateral tire loads in the Sharp corner scenario are given in Tables 4.6 and 4.7.

Table 4.6: Downforce distribution and normal tire load values for the Sharp corner scenario.

Angle [°]	**FDD [%]**	**LDD [%]**	$F_{Z_{FL}}$ **[N]**	$F_{Z_{FR}}$ **[N]**	$F_{Z_{RL}}$ **[N]**	$F_{Z_{RR}}$ **[N]**
0	48.5	65.5	270.8	1164.2	279	1189.1
2.5	50.4	67.1	274.7	1163.7	277.7	1186
5	51	67.7	274.2	1162.6	275.7	1184.2
7.5	51.8	69.7	274.1	1159.7	273.6	1180.5
10	52.1	70.9	274.6	1158.1	273.2	1178.7
12.5	52.9	72.8	275.6	1156.1	272.2	1176.1
15	53.7	73.4	275.4	1155.2	270	1174.5
17.5	54.3	73.2	277.1	1156.1	270	1174.8
20	55	74.5	276.5	1154.1	267.8	1172.6

Table 4.7: Downforce distribution and lateral tire load values for the Sharp corner scenario.

Angle [°]	**FDD** [%]	**LDD** [%]	$F_{Y_{FL}}$ [N]	$F_{Y_{FR}}$ [N]	$F_{Y_{RL}}$ [N]	$F_{Y_{RR}}$ [N]
0	48.5	65.5	459.3	1651.2	472.4	1677.3
2.5	50.4	67.1	465.6	1650.7	470.4	1674.1
5	51	67.7	464.7	1649.5	467.1	1672.2
7.5	51.8	69.7	464.7	1646.4	463.8	1668.3
10	52.1	70.9	465.3	1644.8	463.2	1666.5
12.5	52.9	72.8	467	1642.6	461.5	1663.7
15	53.7	73.4	466.6	1641.6	457.9	1662.1
17.5	54.3	73.2	469.5	1642.6	458	1662.3
20	55	74.5	468.5	1640.5	454.5	1660

The regular decreasing trend of the RW downforce and the fact that the FW downforce stays generally constant is reflected in a regular forward balance shift, with FDD increasing up to almost 6.5%.
The loss of downforce on the right side of the RW causes LDD to increase even more, with a 9% lateral balance shift to the left. This meets Zenvo's findings in behavior, but the shift is much lower than the 30% measured by them.
Both these trends are shown in Figure 4.17.

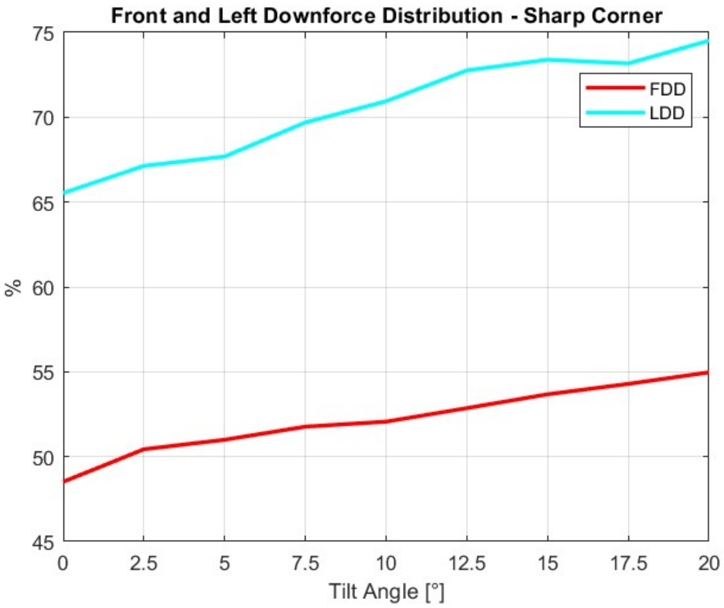

Figure 4.17: FDD and LDD trends for the Sharp corner scenario.

The trends for normal loads on the left and right tires are given in Figure 4.18.

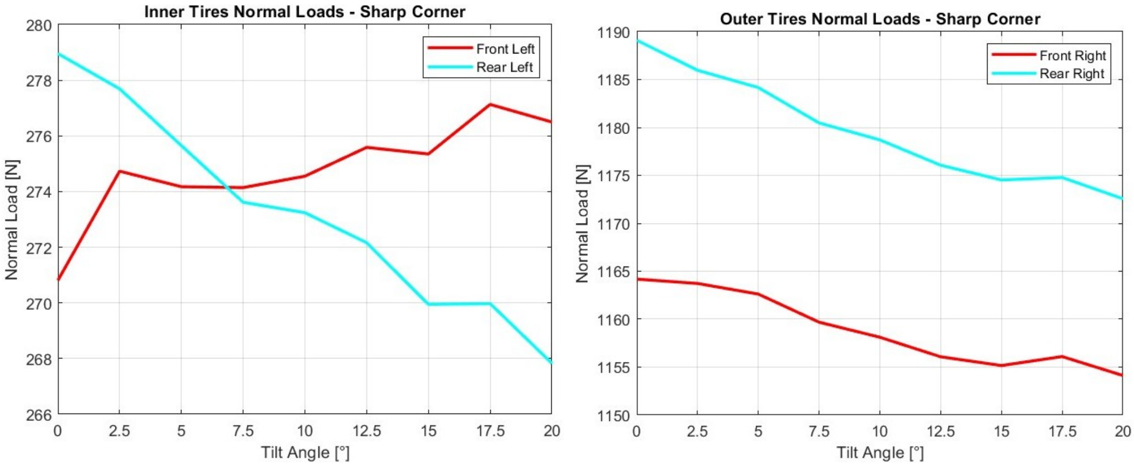

Figure 4.18: Normal tire load trends for the Sharp corner scenario.

Similarly to the Skidpad scenario, the load on the front left tire increases with the tilt angle, this time with an early local maximum followed by a slightly oscillating trend for a final 2% increase. The fact that the normal load on the rear left decreases by 4% - twice as much - might suggest that the front balance shift might be once again predominant over the lateral.

The outer tires lose normal load with an almost linear trend: the load on the rear right decreases more than that on the front right, which is due to both FDD and LDD increasing.

Figure 4.19 shows the trends for the lateral loads generated by the left and right tires.

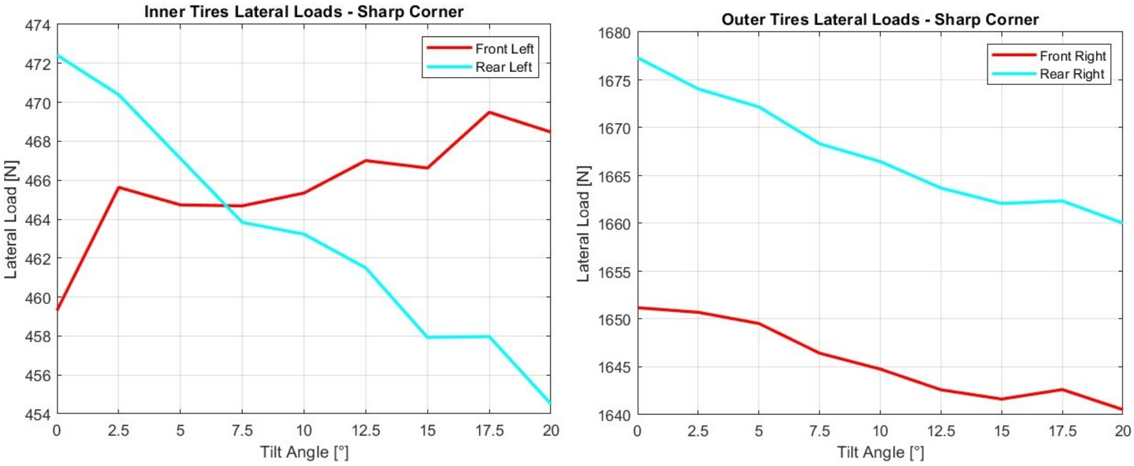

Figure 4.19: Lateral tire load trends for the Sharp corner scenario.

The lateral load trends reflect what was observed in the Skidpad scenario, with lateral loads changing in the same way as normal loads do at each consecutive wing configuration.

4.2.3 Laptimes

The results and trend for the Skidpad laptimes in the Sharp corner scenario are given in Table 4.8 and Figure 4.20.

Table 4.8: Laptimes for the Sharp corner scenario.

Angle [°]	Laptime [s]
0	3.3864
2.5	3.3862
5	3.389
7.5	3.3931
10	3.3945
12.5	3.3965
15	3.3992
17.5	3.3975
20	3.4011

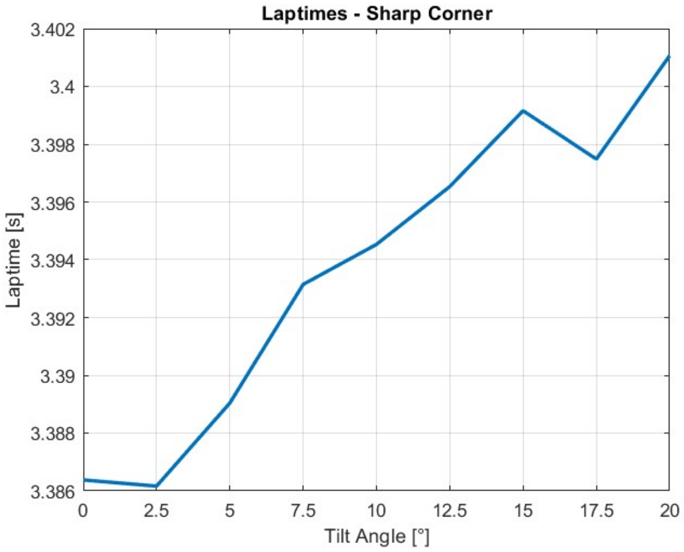

Figure 4.20: Laptime trend for the Sharp corner scenario.

It is clear that implementing the system would not give any improvement in the sharpest possible corner. Laptimes in this scenario are linked to downforce more strongly than they were in the Skidpad case, where some influence from tire load distribution could be noticed, and get higher as the rear wing is tilted.

4.3 Wide corner

The results for the wide corner are presented in this section.

4.3.1 Downforce

Downforce values for the whole car and the specific aerodynamic devices are presented in Table 4.9.

Table 4.9: Downforce values for the Wide corner scenario.

Angle [°]	Total [N]	FW [N]	RW [N]	SW [N]	Diffuser [N]
0	809.2	317.4	221.4	206.5	101.4
2.5	783.4	316	203.5	201.5	101.6
5	791.2	320.1	203.9	201.2	104.2
7.5	818	328.6	210.3	212.1	106.3
10	797.3	313.2	194.2	219.1	109.9
12.5	816.6	327	197.9	221.3	108.1
15	801.7	316.4	197.1	218.7	110.3
17.5	786.7	321.1	179.9	212.6	111.9
20	777.8	313.8	176.1	216.6	109.9

This scenario is the most irregular one, without a visible total downforce trend. Local minimums are found at the 2.5° and 10°-tilt configurations, while local maximums are found at 7.5° and 12.5°.

The lowest value, found at 20°, is just slightly lower than the result at 2.5°.

However, the different devices generally behave in a similar way compared to the Skidpad scenario given in Figure 4.1.

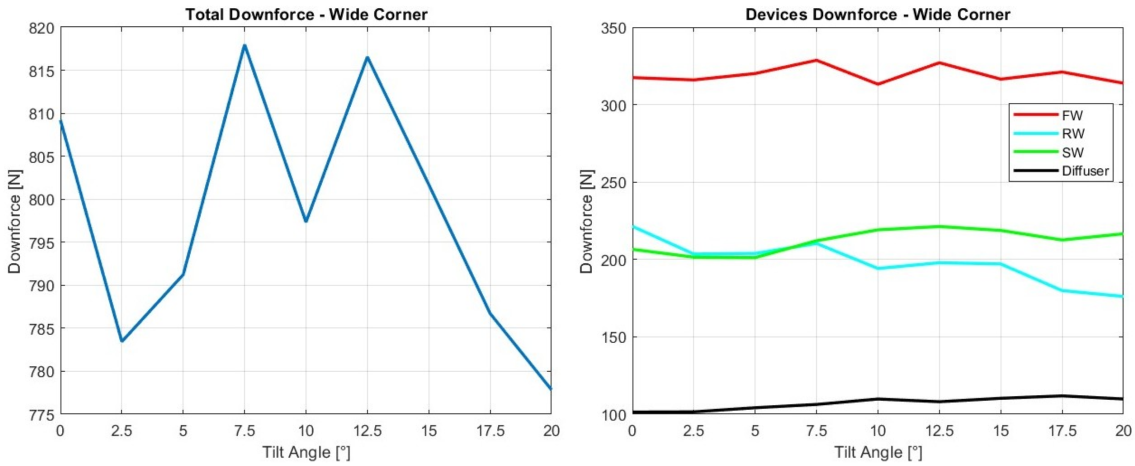

Figure 4.21: Downforce trends for the Wide corner scenario.

Due to the higher flow velocity used in the Wide cornering setup, the downforce graphs show larger variations in absolute numbers compared to the other two scenarios, while still describing limited variations in percentage.

As a reference, it is important to keep in mind the 5.2% RW downforce increase at the 2.5°-tilt configuration in the Skidpad scenario, referable in Figure 4.2, that could only be shown through small details.

In this case, between the two peaks at 2.5° and 7.5°, the FW, SW, RW and diffuser downforce increase by 4%, 5.3%, 3.3% and 4.7% respectively, resulting in only 4.4%

total downforce increase: for this reason, it is almost impossible to notice relevant differences in the flow velocity pictures shown in Figures 4.22 and 4.23 below.
The only visible differences in the wake region around the RW are caused by the different tilt angle, meaning that the section plane cuts the right endplate differently and shows how the flow changes because of it.
Beside this, the flow extraction and wake generated by FW and SW appear very similar in the two configurations, with most of the performance coming from the left side of the car.

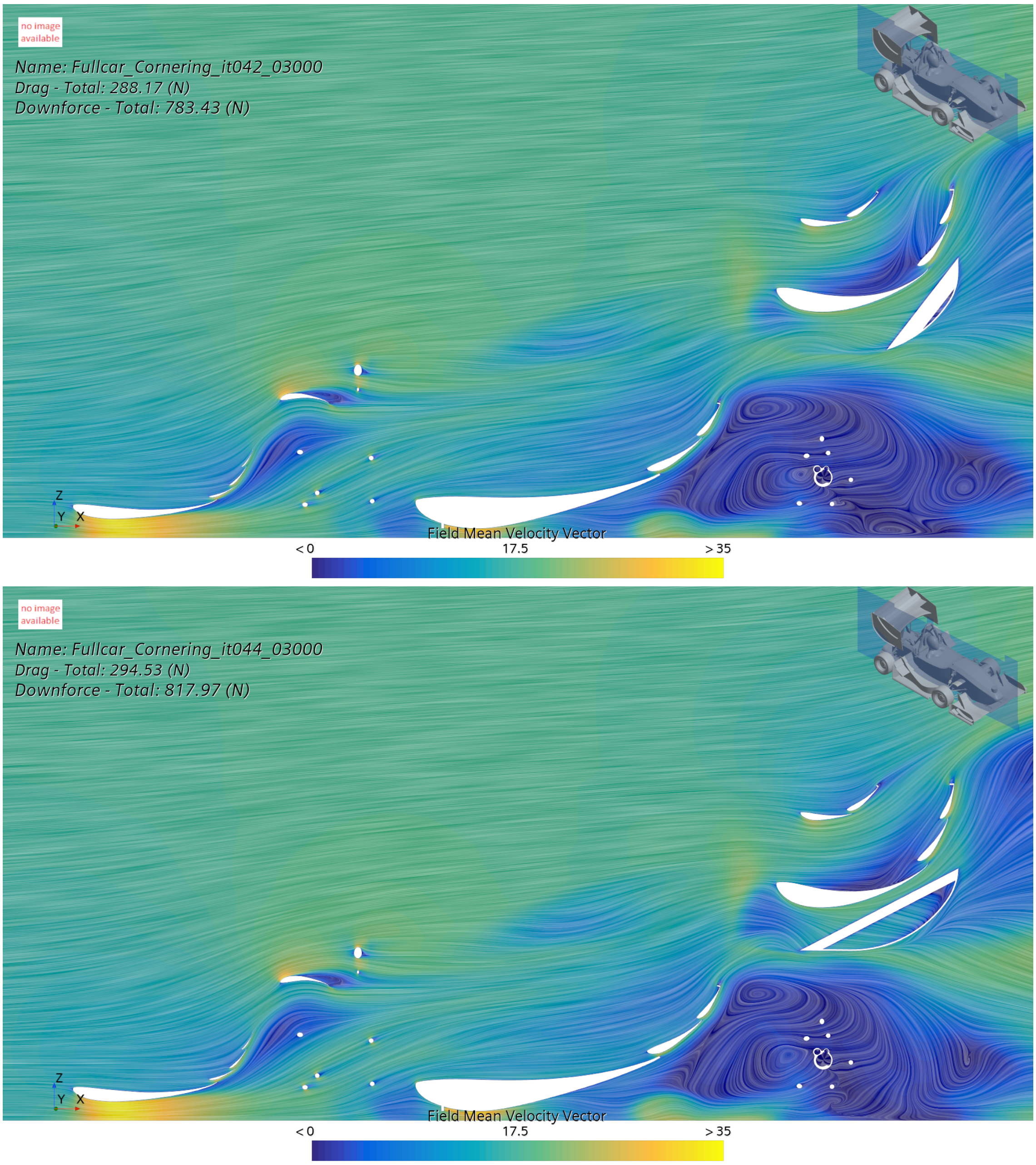

Figure 4.22: Flow velocity pictures for 2.5°-tilt (top) and 7.5°-tilt (bottom) configurations, lateral view, taken 25 cm right of the centerline of the car.

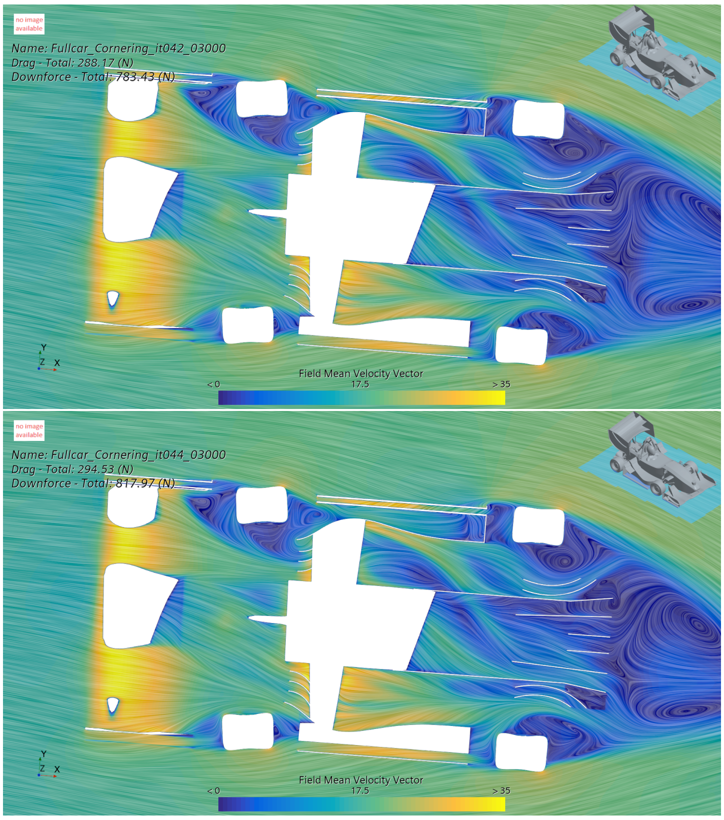

Figure 4.23: Flow velocity pictures for 2.5°-tilt (top) and 7.5°-tilt (bottom) configurations, top view, taken 6 cm above the ground.

The RW downforce trend decreases as expected, with slight oscillations as previously mentioned. Figures 4.24 and 4.25 below show that, unlike the previous scenarios, now lifting the left side in the 20°-tilt configuration does not induce any local downforce increase; the lowered right side, instead, ends up working in a low-energy region and causes a general downforce decrease.

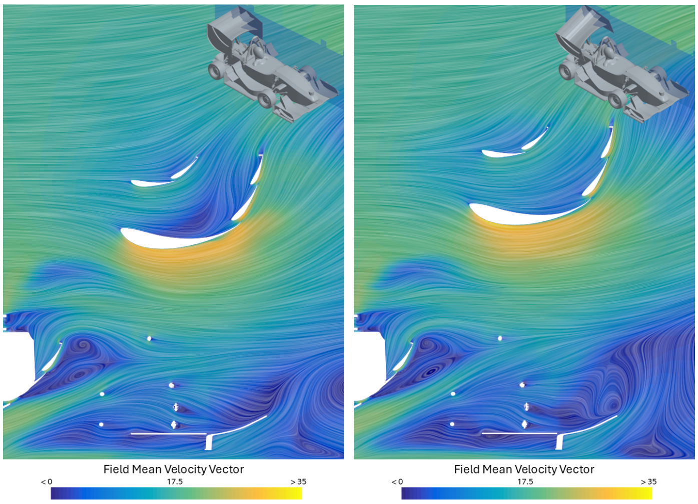

Figure 4.24: Flow velocity pictures for no-tilt (left) and 20°-tilt (right) configurations, lateral view, taken 20 cm left of the centerline of the car.

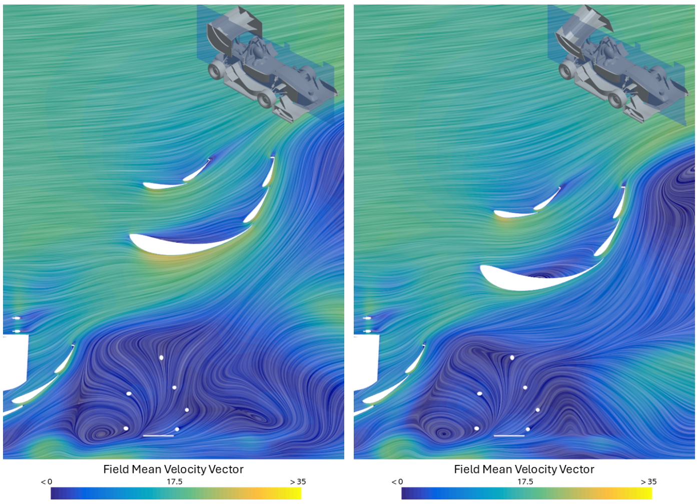

Figure 4.25: Flow velocity pictures for no-tilt (left) and 20°-tilt (right) configurations, lateral view, taken 20 cm right of the centerline of the car.

What emerges from Figure 4.25 is a difference in the low rear wake, with an inwash similar to that noted in the previous scenarios but less intense, as visible in Figure 4.26 below.

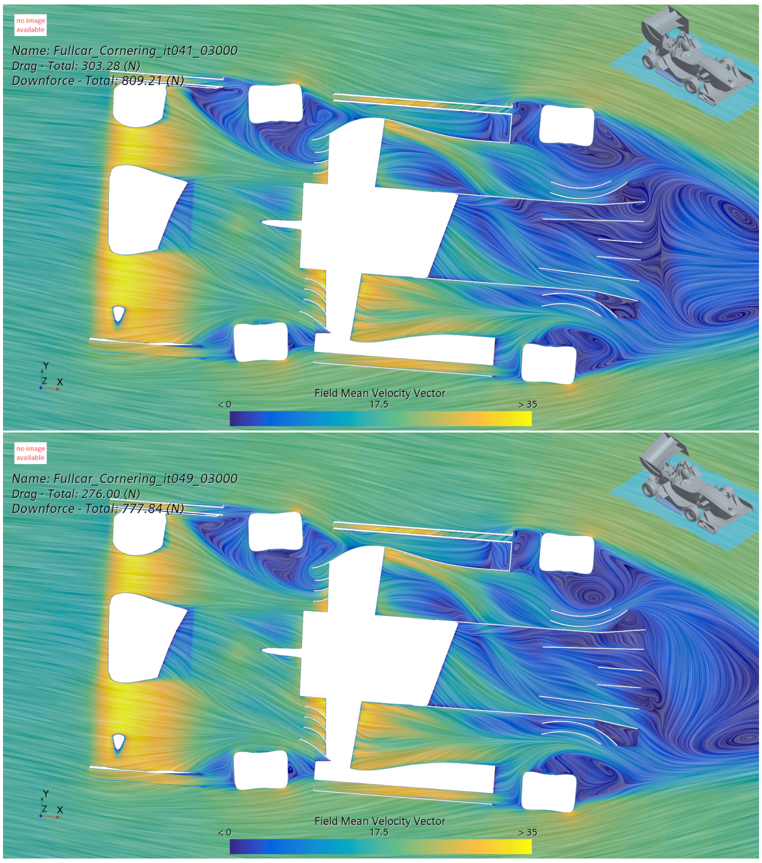
Name: Fullcar_Cornering_it041_03000
Drag - Total: 303.28 (N)
Downforce - Total: 809.21 (N)

Name: Fullcar_Cornering_it049_03000
Drag - Total: 276.00 (N)
Downforce - Total: 777.84 (N)

Figure 4.26: Flow velocity pictures for no-tilt (top) and 20°-tilt (bottom) configurations, top view, taken 6 cm above the ground.

The smaller steering angles of the front tires allow more high-energy air to flow under the SW, especially the right one as can be seen in Figure 4.26.
The same figure shows that, similarly to the previous scenarios, the flow through the FW underbody is highly unbalanced to the left, leading to the left SW to generate most of the downforce.

4.3.2 Downforce distribution and tire loads

The results for the front and left downforce distribution and the normal and lateral tire loads in the Wide corner scenario are given in Tables 4.10 and4.11.

Table 4.10: Downforce distribution and normal tire load values for the Wide corner scenario.

Angle [°]	**FDD** [%]	**LDD** [%]	$F_{Z_{FL}}$ [N]	$F_{Z_{FR}}$ [N]	$F_{Z_{RL}}$ [N]	$F_{Z_{RR}}$ [N]
0	57.2	60	451.7	1346.3	385.7	1323.4
2.5	59.3	61.2	458.6	1341.7	372.6	1308.3
5	59.9	61.6	465.8	1343.2	373.3	1306.7
7.5	60	61.5	475.9	1350.1	379.1	1310.7
10	60.5	62.6	476.4	1341.4	375	1302.3
12.5	61.4	62.5	487.9	1349.1	374.7	1302.6
15	60.4	63.9	483.8	1335.8	380.7	1299.1
17.5	62.2	65.2	493.3	1331.1	371.9	1288.1
20	62.5	65.2	491.1	1330.1	368.2	1286.2

Table 4.11: Downforce distribution and lateral tire load values for the Wide corner scenario.

Angle [°]	**FDD** [%]	**LDD** [%]	$F_{Y_{FL}}$ [N]	$F_{Y_{FR}}$ [N]	$F_{Y_{RL}}$ [N]	$F_{Y_{RR}}$ [N]
0	57.2	60	740.6	1833.2	640.4	1811.5
2.5	59.3	61.2	751.1	1828.9	620.2	1797
5	59.9	61.6	761.8	1830.3	621.3	1795.4
7.5	60	61.5	776.8	1836.8	630.2	1799.3
10	60.5	62.6	777.6	1828.7	623.9	1791.2
12.5	61.4	62.5	794.6	1835.9	623.4	1791.5
15	60.4	63.9	788.5	1823.4	632.7	1788.1
17.5	62.2	65.2	802.6	1818.9	619.2	1777.3
20	62.5	65.2	799.3	1817.9	613.3	1775.4

As visible in Figure 4.27, both FDD and LDD still follow an increasing trend, with a final increase of approximately 5.3% for both, but now present several irregularities and, for FDD, a local minimum at the 15°-tilt configuration.
This is explained by the fact that for that specific configuration the downforce generated by the FW decreases while that generated by the RW stays constant, thus causing the balance to shift backwards.

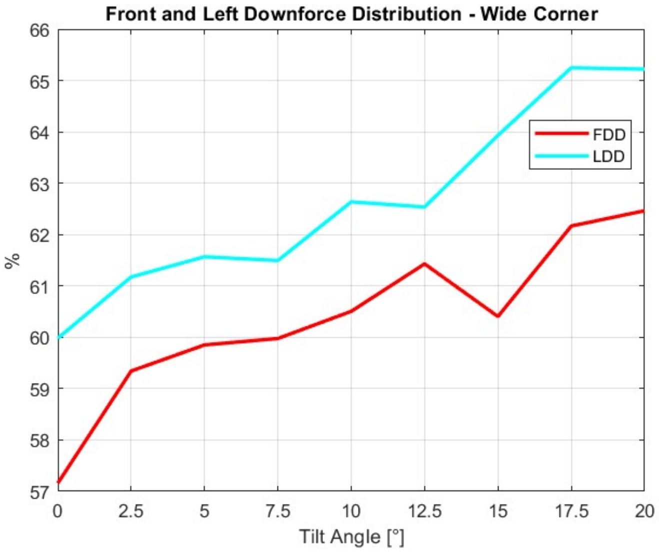

Figure 4.27: FDD and LDD trends for the Wide corner scenario.

The trends for normal loads on the left and right tires are given in Figure 4.28

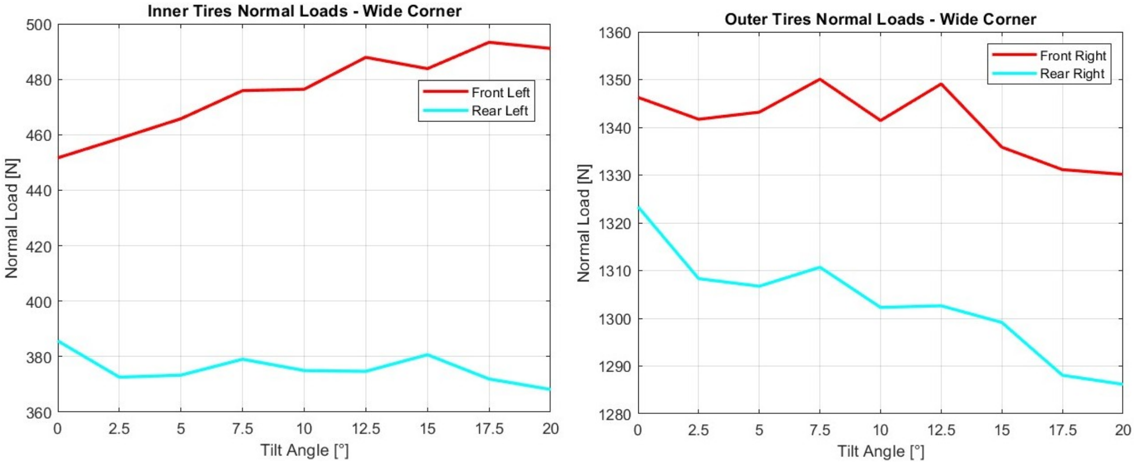

Figure 4.28: Normal tire load trends for the Wide corner scenario.

The load on the front left tire increases with some oscillations, feeling the influence of both FDD and LDD, and reaches a final increase of 8.8%.
Similarly to the Skidpad scenario, the rear left tire graph oscillates around the baseline value and shows dependance to the front balance more than to the left balance: it is interesting to see, as an example, that despite balance moves more left than forward between 7.5° and 10°, the rear left tire still sees a decreased normal load.
The outer tires also show irregular decreasing trends, with the front left strongly depending on the FW downforce, as it appears to be resembling its local minimum and maximums especially between 7.5° and 12.5°.

Shown in Figure 4.29 are the trends for the lateral loads generated by the inner and outer tires in the Wide corner scenario.

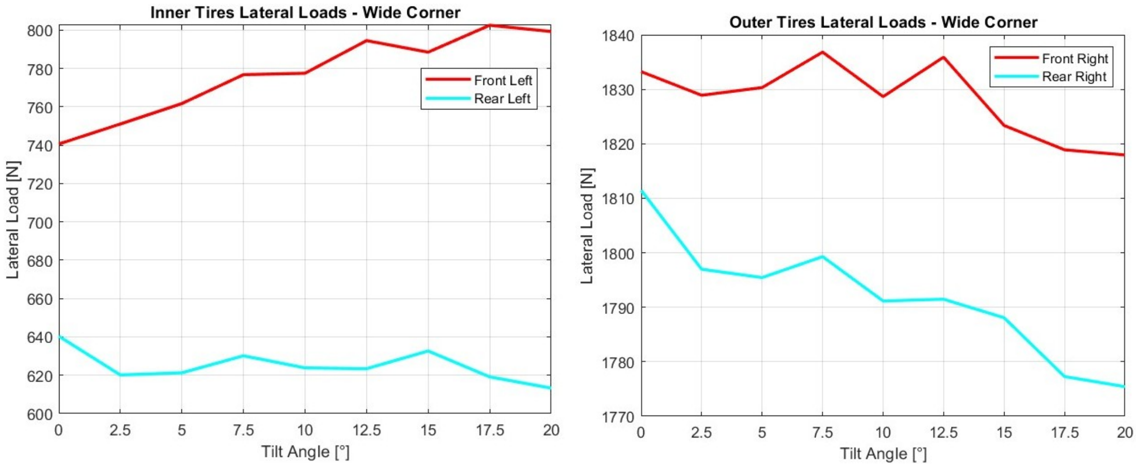

Figure 4.29: Lateral tire load trends for the Wide corner scenario.

Again, the pictures show that the lateral and normal loads relative to each tire vary in the same way.

4.3.3 Laptimes

The results and trend for laptimes in the Wide corner scenario are given in Table 4.12 and Figure 4.30.
Similarly to the Skidpad findings, the graph shows a strong dependency of laptimes on the total downforce, getting higher at low downforce configurations and vice versa. The largest gain (12 ms) is found with the 12°-tilt configuration. Interestingly, the 20°-tilt configuration no longer gives the slowest laptime. The 2.5°-tilt configuration showed very low downforce and not the most left and forward load balance, meaning that at 20°, despite the overall lowest downforce, load balance plays a role in improving the cornering performance of the car. The largest gain, 12 ms at the 15°-tilt configuration, represents the highest improvement obtained among the three different cases with the CFS25 tires. However, Section 4.5 will show that implementing this system for such a relatively small improvement might not be worth it.

Table 4.12: Laptimes for the Wide corner scenario.

Angle [°]	**Laptime [s]**
0	6.2357
2.5	6.2535
5	6.2462
7.5	6.2249
10	6.2385
12.5	6.2235
15	6.2314
17.5	6.2405
20	6.2479

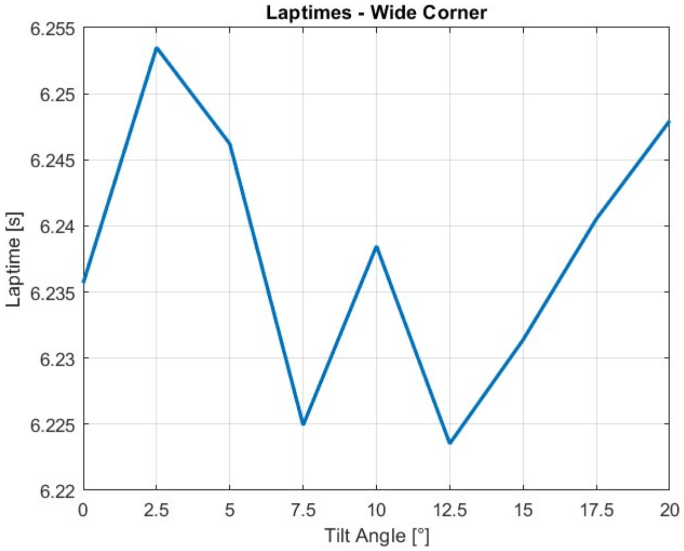

Figure 4.30: Laptime trend for the Wide corner scenario.

4.4 Rear Wing comparison between CFD and theoretical expectations

The expected behavior of the RW downforce, discussed in Section 2.4, would be a continuous regular decrease dependent on the tilt angle. The comparison between expected behavior and CFD findings for each scenario is shown in Figure 4.31.

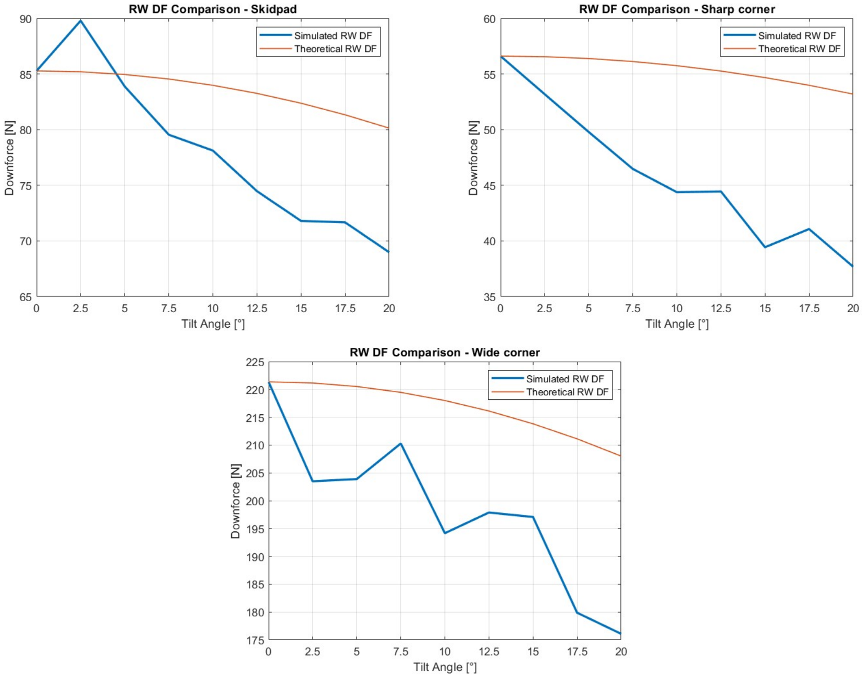

Figure 4.31: Comparison between theoretical and simulated RW downforce in the Skidpad (top left), Sharp (top right) and Wide (bottom) corner scenario.

Downforce decreases as expected, except for the already analyzed local increase in Skidpad, but with different trends and different magnitudes in each scenario. While the theoretical trend shows a final 6% decrease, the simulated data results in a 18%, 33.3% and 20.4% decrease for the Skidpad, Sharp and Wide corner scenarios respectively.

This clearly shows the influence that the presence of other elements and aerodynamic devices has on the RW behavior, that is not only related to the tilt angle but also to how the flow changes around it.

4.5 Lateral loads and laptimes with more load sensitive tires

The validity of the system with more load sensitive tires was tested in each scenario using three different tire models, illustrated in Figure 4.32, as data for the 6" CFS24 tires was not available.

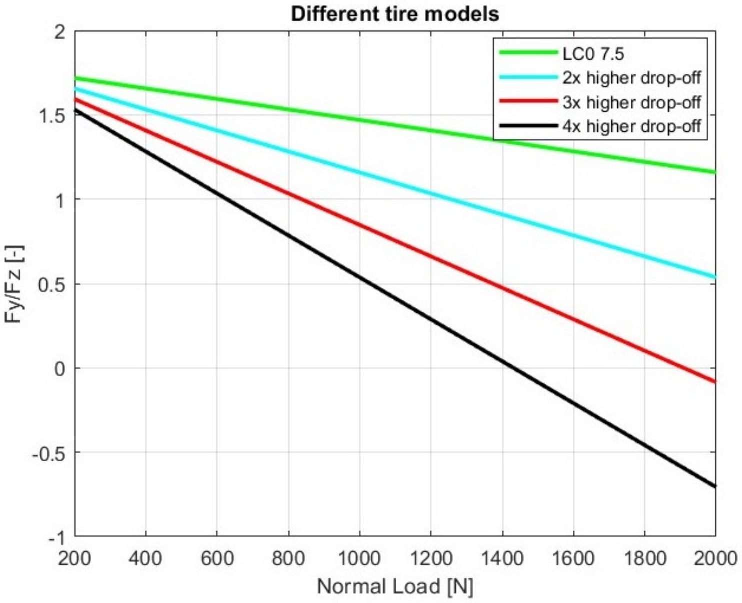

Figure 4.32: Comparison between the load sensitive tire models and LC0 7.5.

The models present a drop-off (decrease of friction coefficient as function of normal load) two, three and four times higher than that of the original LC0 7.5, respectively. Each of the following three sections features a discussion on how lateral loads change when tires are more sensitive to normal loads, and the laptimes achieved are shown to ultimately assess eventual benefits.

4.5.0.1 Skidpad corner

The lateral loads generated by each tire in the Skidpad scenario are shown in Figures 4.33, 4.34 and 4.35.

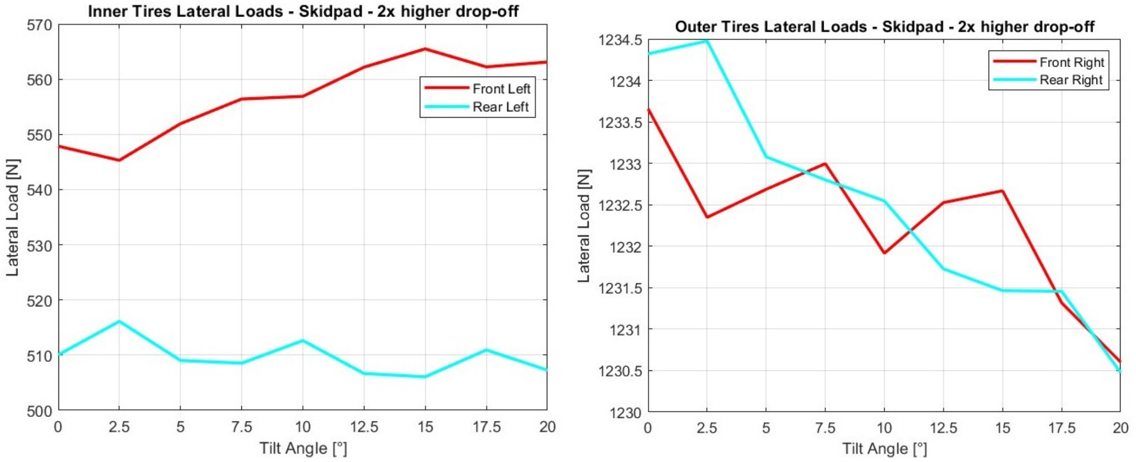

Figure 4.33: Lateral tire load trends for the Skidpad scenario, 2x worse tires.

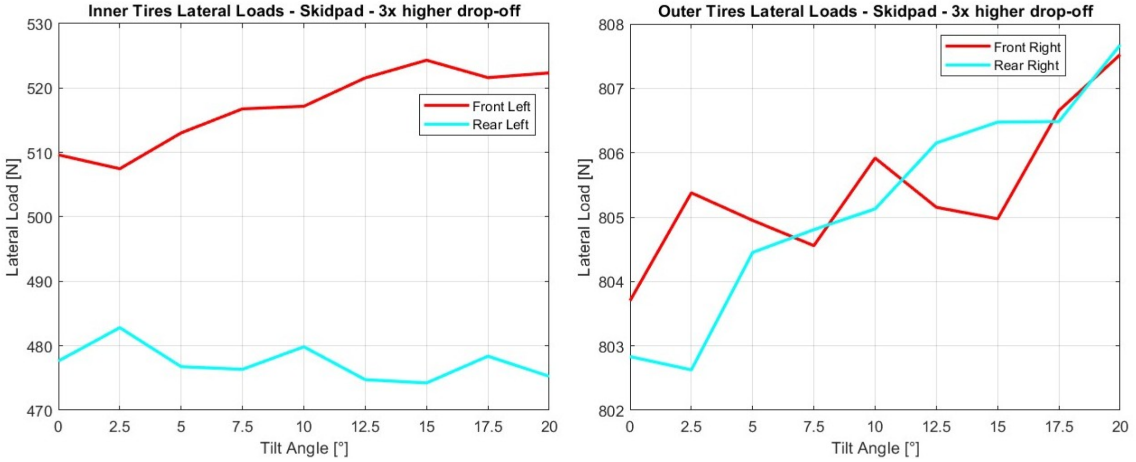

Figure 4.34: Lateral tire load trends for the Skidpad scenario, 3x worse tires.

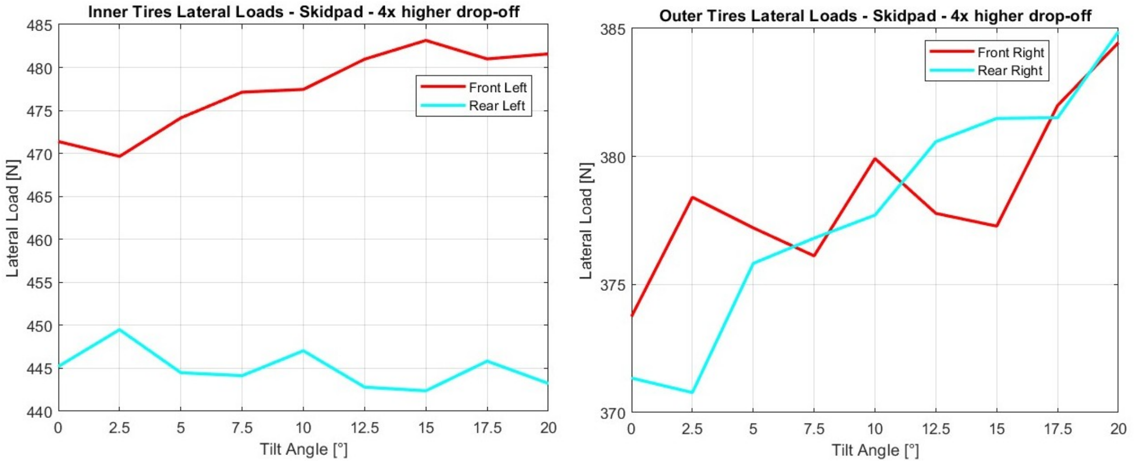

Figure 4.35: Lateral tire load trends for the Skidpad scenario, 4x worse tires.

As expected, the lateral load generated by each tire decreases as the drop-off increases. What is interesting to note is that while the inner tires keep showing the same trends, for three and four times higher drop-off the graphs for the outer tires get perfectly flipped upside down. Completely tilting the RW when the car is equipped with tires at least three times worse than LCO 7.5 would result in an increase of the lateral load generated by the tires, even if the loads are obviously lower due to the tires being generally less performant.

The laptimes achieved in each case are presented in Figures 4.36, 4.37 and 4.38.

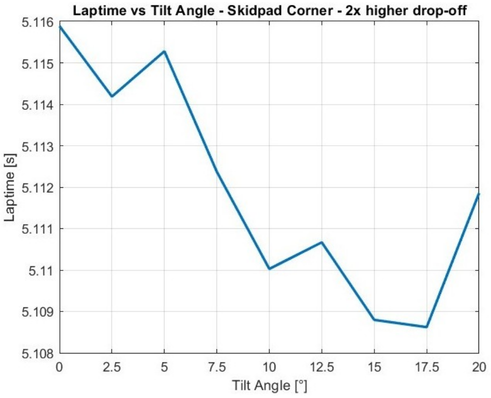

Figure 4.36: Laptime trends for the Skidpad scenario, 2x worse tires.

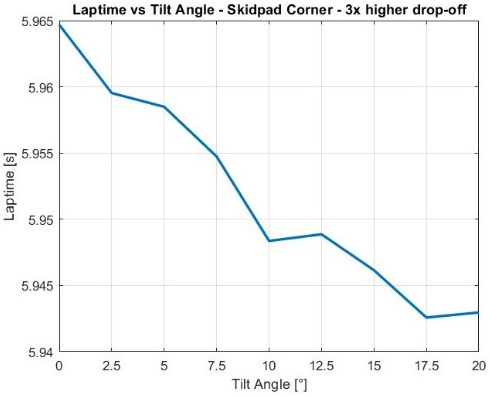

Figure 4.37: Laptime trends for the Skidpad scenario, 3x worse tires.

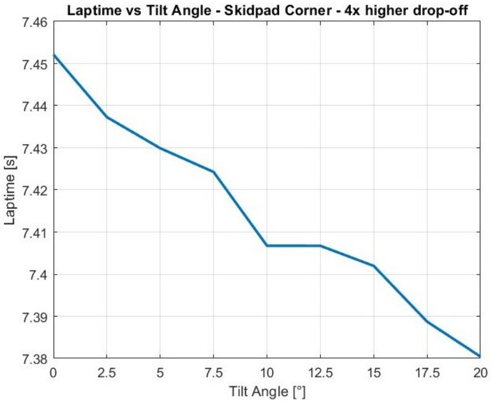

Figure 4.38: Laptime trends for the Skidpad scenario, 4x worse tires.

According to the laptime graphs it would take a three-times higher drop-off to get a first consistent laptime gain trend, with a maximum gain of 23 ms, while using a four-times worse tire would give a 72 ms gain at the 20°-tilt configuration.
This is because with such load sensitive compounds both front tires generate increased grip and therefore lateral loads, which means that the car's performance in cornering is improved.

This, clearly, at the expense of higher laptimes due to overall lower lateral loads generated and cornering speeds achieved, therefore the system would be only useful for cars equipped with tires affected by at least a three-times higher drop-off than CFS.

4.5.0.2 Sharp corner

The lateral loads generated by each tire in the Sharp corner scenario are shown in Figures 4.39, 4.40 and 4.41.

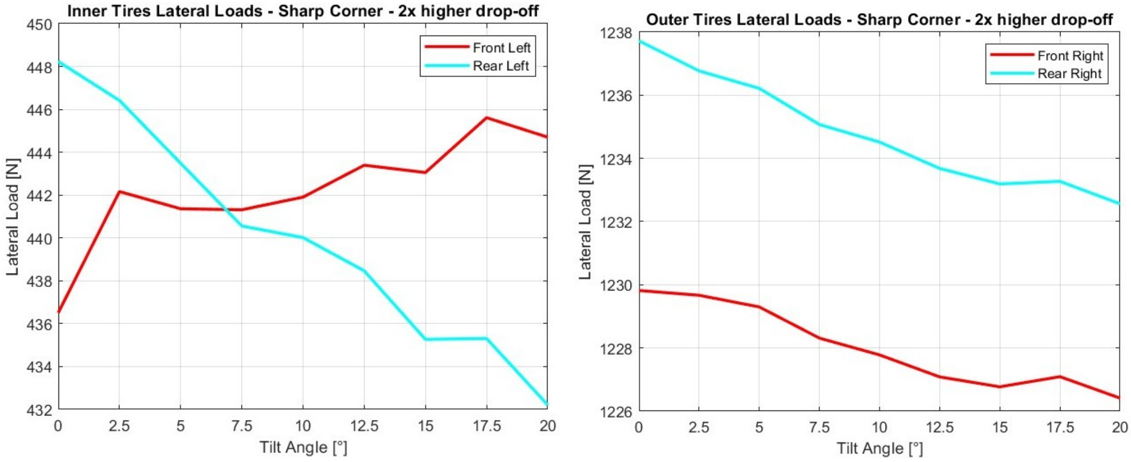

Figure 4.39: Lateral tire load trends for the Sharp corner scenario, 2x worse tires.

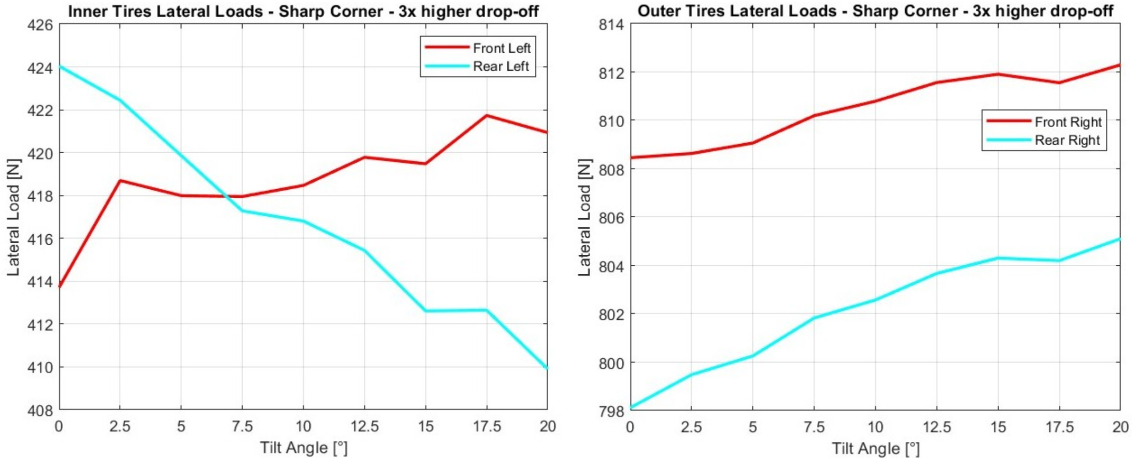

Figure 4.40: Lateral tire load trends for the Sharp corner scenario, 3x worse tires.

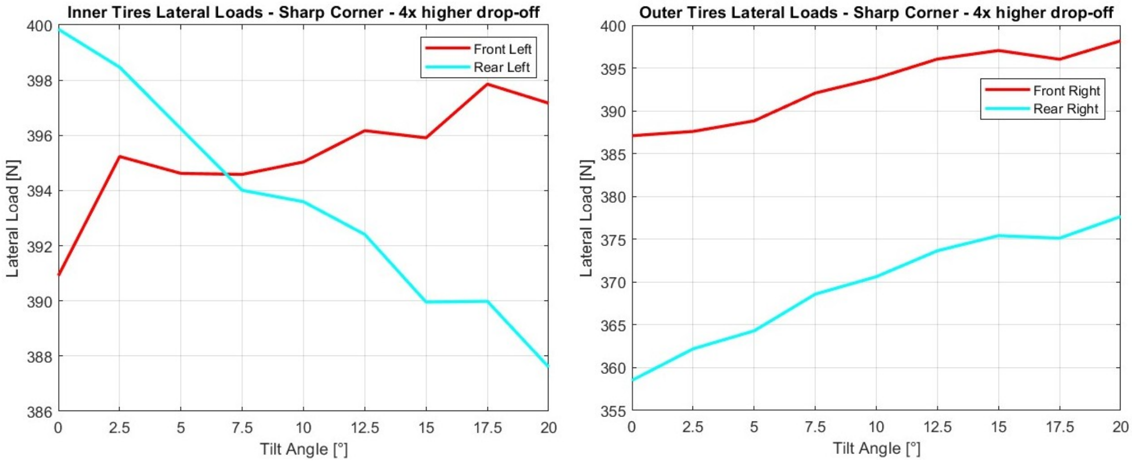

Figure 4.41: Lateral tire load trends for the Sharp corner scenario, 4x worse tires.

Similarly to what emerged from the previous scenario, a three-times higher drop-off causes the lateral load trends for the outer tires to flip, for a general increase in the load generated as the RW is tilted.

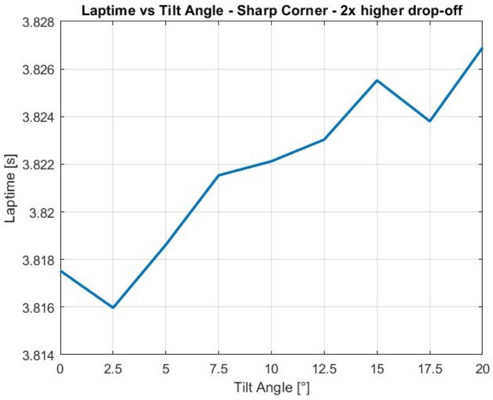

Figure 4.42: Laptime trends for the Sharp corner scenario, 2x higher drop-off.

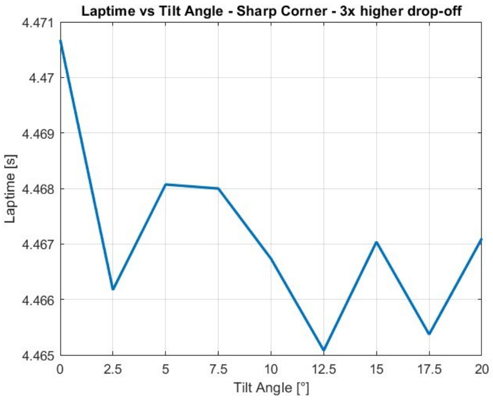

Figure 4.43: Laptime trends for the Sharp corner scenario, 3x higher drop-off.

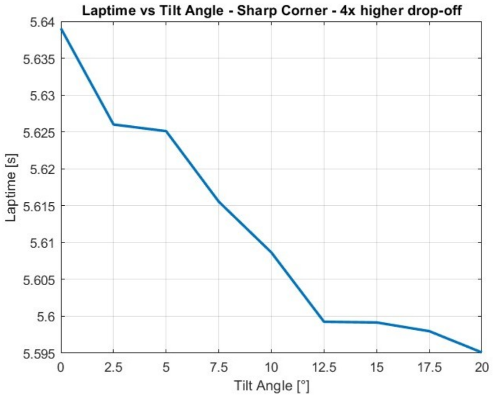

Figure 4.44: Laptime trends for the Sharp corner scenario, 4x higher drop-off.

It appears that to get some improvements a three-times higher drop-off would be necessary, similarly to the Skidpad scenario, but a four-times higher drop-off is needed to obtain the first monotonous trend and a gain of 45 ms.
This is mostly due to the more oscillatory behavior of the lateral load generated by the front inner tire, that decreases for some RW configurations: when, as in the four-times higher drop-off case, the difference in loads between consecutive configurations gets smaller, the improvements on the outer front tire slightly prevail and laptimes slightly improve.

4.5.0.3 Wide corner

The lateral loads generated by each tire in the Wide corner scenario are shown in Figures 4.45, 4.46 and 4.47.
Once again, the lateral load graphs for the outer tires show an inverse behavior compared to the LCO 7.5 tire and a two-times worse tire compound.

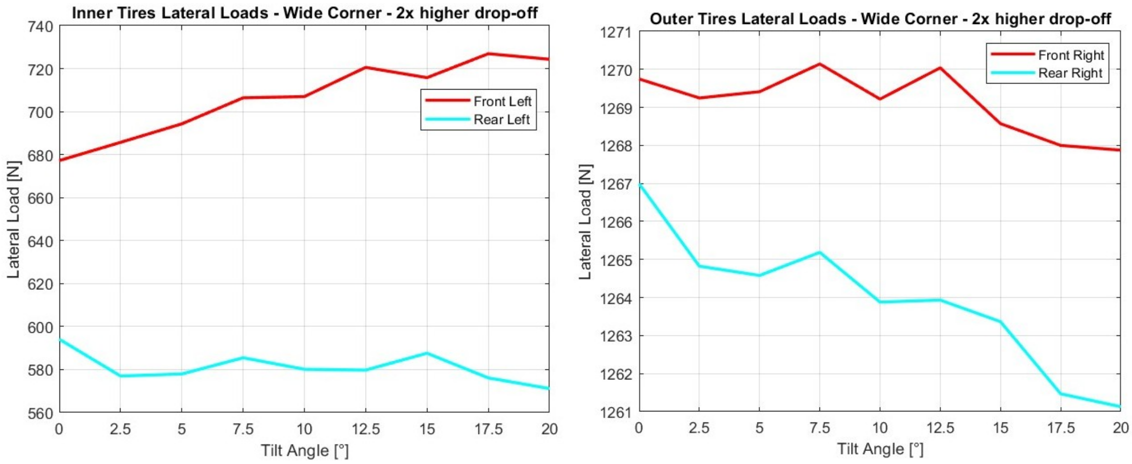

Figure 4.45: Lateral tire load trends for the Wide corner scenario, 2x worse tires.

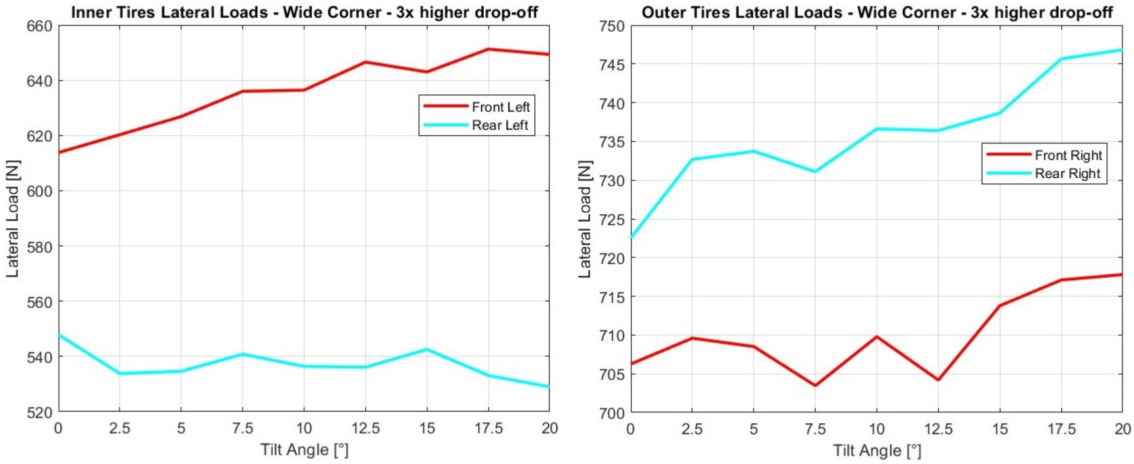

Figure 4.46: Lateral tire load trends for the Wide corner scenario, 3x worse tires.

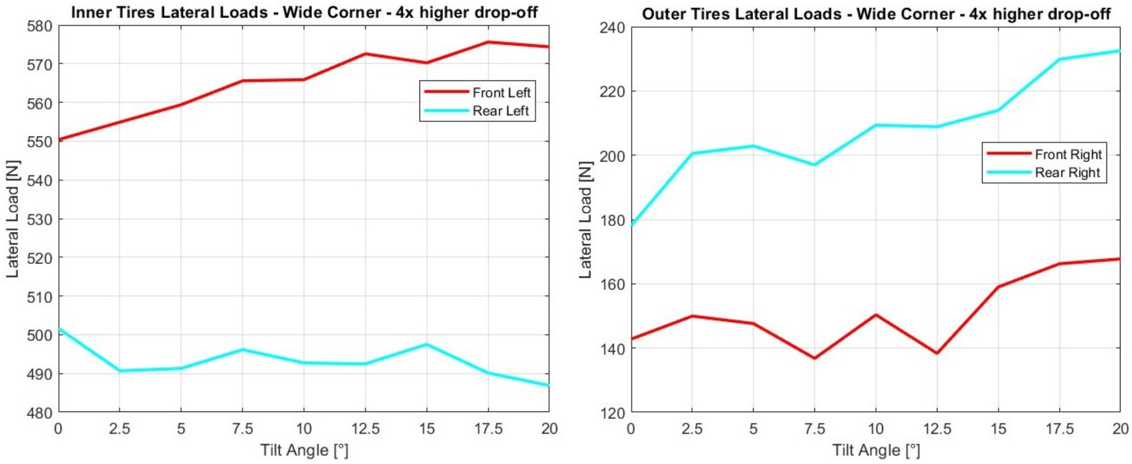

Figure 4.47: Lateral tire load trends for the Wide corner scenario, 4x worse tires.

The resulting laptimes are given in Figures 4.48, 4.49 and 4.50.

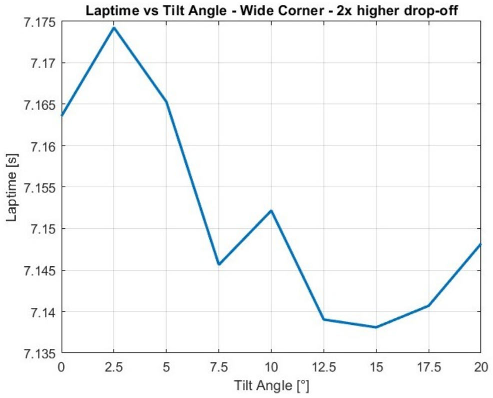

Figure 4.48: Laptime trends for the Wide corner scenario, 2x worse tires.

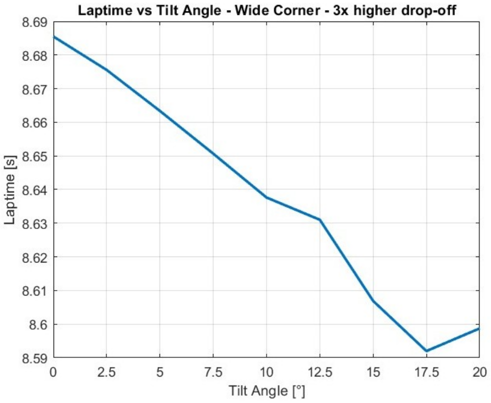

Figure 4.49: Laptime trends for the Wide corner scenario, 3x worse tires.

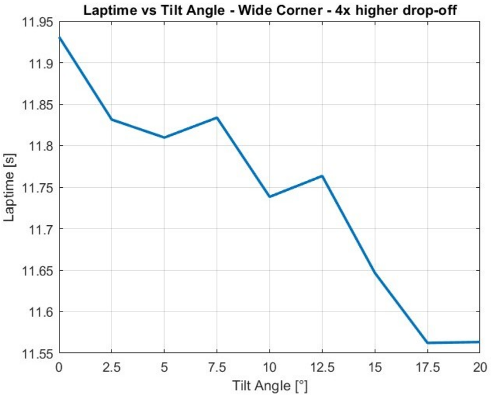

Figure 4.50: Laptime trends for the Wide corner scenario, 4x worse tires.

It would take tires with a three-times higher drop-off to get a regular decreasing laptime trend, while a four-times higher drop-off would give an irregular trend instead. This is because the negative oscillations in the outer front tire graph in Figure 4.47 prevail over the generally increasing trend of the front inner, resulting in less grip and worse performance.
The maximum gain, with three times worse tires, would now be nearly a tenth of a second, at the 17.5°-tilt configuration.

4.6 Contextualization of laptime gains

The laptime gains obtained in the simulated Skidpad scenario, both with the CFS25 tires and with the made-up worse tire models, are compared with the Manual Skidpad event CFS has participated in at FSG 2024. This is done to contextualize results and be able to state whether a gain is acceptable or not given the gaps between teams, and therefore whether it is worth it or not to consider the implementation of this system on a real CFS car.

The Skidpad event consists of two full circles, one clockwise and one counterclockwise, to be completed: the two laptimes are then averaged and give the final laptime.

Table 4.13 shows a timetable where only the best valid time recorded by each team in a single full circle is listed; the timetable stops at CFS, as it is not important to consider worse laptimes.
The timetable is therefore not official, does not reflect the final placement of the teams, as averaged times are not considered, and only serves the purpose of giving an idea of what can be defined a useful gain.

Table 4.13: FSG 2024 Skidpad timetable. [12]

P	Team	Laptime [s]
1	Dresden TU	4.61
2	Milano PT	4.67
3	Zürich ETH	4.75
4	Tallinn TU UAS	4.77
5	Nürnberg GSO UAS	4.78
6	München UAS	4.80
7	Stuttgart DHBW	4.80
8	Eindhoven TU	4.82
9	Karlsruhe KIT	4.84
10	Amberg OTH	4.86
11	Esslingen UAS	4.88
12	Aachen RWTH	4.94
13	Göteborg Chalmers	4.95

It is important to note that the simulated laptime at the no-tilt configuration, 4.5497 s, is much faster than any of the real laptimes. This gives an idea of the impact that the simplifications in the methods used, as well as the driver's capabilities, can have over the correlation between simulation data and real on-track performance.

Clearly the fact that worse tires give much slower laptimes is not considered, as the intent of this section is to merely illustrate different types of laptime gains, and it must not be concluded that mounting this system with worse tires is a worthwile approach.

4.6.1 LC0 7.5

The largest gain for the baseline Skidpad scenario, as already mentioned in Section 4.1.3, is 1.7 ms obtained at the 15°-tilt configuration.
This is clearly an insufficient gain as it would be impossible for CFS to overtake any other team.

4.6.2 Load sensitive tires

The first notable improvement is obtained with a compound that is three times worse than the current CFS tires, with a 22.1 ms gain. This would allow CFS to overtake Aachen and, in general, to any of the mid-table teams to overtake, or at least close the gap with, the first team just ahead of them.

The largest gain obtained with the worst tire model is 71.7 ms. With such gain it would be possible for CFS to gain one or even two positions, depending on the real Esslingen time, while faster teams would be able to overtake several opponents; as an example, Milano would win and Eindhoven would fight for the podium. This represents the type of laptime improvement that would justify the implementation of the system, but the impact that other factors not taken into account in the development of this project is discussed in the Conclusion chapter.

5

Conclusion

This chapter presents a summary of the results found through the project and their meaning, followed by a discussion over important aspects that have been ignored to simplify the process; an overview of potential future works is given in the last section.

5.1 Summary of results

Tilting Svea's rear wing laterally gives a general decrease in downforce and a lateral load transfer shift, meeting what expected by Zenvo's Centripetal Wing. The magnitude of these phenomenons is, however, very different from what the company claims to have achieved on the TSR-S.
The lower lateral load transfer generated, together with a much higher downforce decrease, would make this system highly inefficient on the CFS25 car. This is mostly due to the mutual influence that the rear wing and the rest of the aerodynamic package have on each other, and to the fact that a road car and a Formula car are two profoundly different concepts, with different shapes and different dynamics.

It was shown that, with high-performance tires like those mounted on Svea, tilting the rear wing would result in a loss of grip on the front outer tire, which agrees with the main concerns coming from the automotive industry. [4]

The interactions between downforce, balance and tire loads generate some slight laptime gains at different RW configurations in Skidpad and wider corners, but the oscillations in results make the system not reliable enough. Moreover, no improvement was found for sharp corners, which is where improvements would be needed the most: this represents another relevant concern regarding the Centripetal Wing.

Regular noticeable improvements were found when mounting a much worse and more load sensitive tire compound. This could justify the implementation of the system when using different tires is not allowed, but for Formula Student teams it would be much easier, safer and less expensive to just use better tires.

5.2 Impact and implications of simplifications

Several aspects were ignored during the development of this project due to limited time and resources, but they would all have an impact over the real performance of the system and the possibility of actually installing it on a FS car.

To be able to rotate the wing, as mentioned in the Methods chapter, a new set of mounting assembly would be needed, requiring a different rigid support compared to what is currently used by CFS, including a set of actuators to change the wing's angle. This would generate a considerable increase in terms of weight, most likely inducing a balance shift towards the rear of the car and thus different vehicle dynamics, that would need to be properly analyzed.

The system would also require a dedicated electronic architecture to make the actuators receive an input from the steering wheel and rotate the wing, which comes with increased costs, manufacturing time and effort, and risks of malfunctions.

5.2.1 FSG Rules

It needs to be mentioned that the current FSG regulations make it, if not forbidden, at least borderline to install such a system on a competing car.
Three rules, individuated in the official rulebook [5] and discussed below, generate the main concerns.

5.2.1.1 Spatial restrictions

The rule T8.2: Restrictions for Aerodynamic Devices regulates the positioning of specific devices mounted on the car; those that have an impact on this system are listed here.

- T8.2.1 Height restrictions: All aerodynamic devices rearward of a vertical plane through the rearmost portion of the front face of the driver head restraint support, excluding any padding, set to its most rearward position must be lower than 1.2 m from the ground.

- T8.2.2 Width restrictions: All aerodynamic devices higher than 500 mm from the ground, must not extend outboard of the most inboard point of the rear wheel/tire.

In simpler terms, the maximum allowed height of the rear wing from the ground is 1.2 m, and it cannot extend beyond the inner face of each rear tire in width.
Since Svea's rear wing is placed inside the mentioned margins just by a few millimeters, tilting it would imply exceeding the limits in both height and width while driving.
It could be argued, however, that other devices already exceed spatial limitations during dynamic events: as an example, front wings scraping on the track in braking maneuvers result in a temporary null ground clearance while driving, and this

is not considered during the mechanical scrutineerings after each event where only the static setup is judged. For the same reason, the system might then be ruled as legal.

5.2.1.2 Rigidity regulations

The rule T8.3: Aerodynamic Devices Stability and Strength regulates the maximum allowed deflections an aerodynamic device must sustain during mechanical scrutineering. In particular:

- T8.3.1: Any aerodynamic device must be able to withstand a force of 200 N distributed over a minimum surface of 225 cm^2 and not deflect more than 10 mm in the load carrying direction.

This restriction is commonly verified by placing sandbags on one side of a device, for a total of 20 kg. Since the implementation of this system requires two actuators to be mounted under the rear wing, it is necessary to install a system of actuators powered only by electric inputs. In this way the wing would only rotate when the actuators receive an input from the steering wheel angle, and it would resist during mechanical scrutineering.

5.2.1.3 Post-inspection modifications

The rule IN1.5 Modifications and Repairs states, for what concerns the rear wing object of this study, that:

- IN1.5.1: After technical inspection, the only modifications allowed to the vehicle are [...] adjustment of winglet angles, but not the position of the complete aerodynamic device in relation to the vehicle

While this rule allows the use of either manual and automated DRS systems, it is the rule that most likely would deem such an active rear wing illegal. It could be argued that no manual modifications are ever performed on the device, that moves while driving and goes back to its initial position when the car stops and gets inspected again, but it is uncertain whether judges would accept such an explanation or not.

5.3 Final verdict

While this system could be useful in normal race cars or hypercars, where the rear wing would almost work as a stand-alone isolated device, given the results and implications discussed above it is safe to say that the implementation of an active rear wing of this type in a CFS car would not be worth the extra costs, manufacturing and, most importantly, the risk of being disqualified from competitions due to an allegedly illegal device.

5.4 Future research

A study over the actuation system required to tilt the rear wing, together with a cost and added weight analysis, would integrate this project and provide a complete overview of all the implications coming from the implementation of such an active aerodynamic device.

The rotation of the Centripetal Wing around the lateral axis, to increase its angle of attack during braking maneuvers, has not been considered in this project.
This might be the best way of implementing an active rear wing on a CFS car, as it would imply rather simpler phenomena and could be tuned in a better way.
Implementing both rotations simultaneously to simulate the actual Centripetal Wing would be a more advanced step, but it would also be much more complex.

Finally, both rotations could be tested independently on a road car similar to the TSR-S, or even the TSR-S itself, to verify the behavior of such system on a different type of vehicle and assess whether Zenvo's claims can be trusted or not.

Bibliography

[1] *Chalmers Formula Student website.* `https://www.chalmersformulastudent.se/garage`

[2] *Formula Student Germany website.* `https://www.formulastudent.de/academy/academy-on-site/2024`

[3] Superbilen. (2018). *Danska superbilen Zenvo TSR-S.* `https://www.sportbilen.se/2018/03/06/danska-superbilen-zenvo-tsr-s/`

[4] Pruett, M. (2018). *Zenvo's Crazy Tilting Rear Wing Would Make a Car Handle Worse.* `https://www.roadandtrack.com/new-cars/car-technology/a21081048/zenvos-tsrs-rear-wing-analysis/`

[5] *Formula Student Germany 2025 Rules.* `https://www.formulastudent.de/fileadmin/user_upload/all/2025/rules/FS-Rules_2025_v1.1.pdf`

[6] Jacobson, B., & Jonasson, M., & Bruzelius, F. (2024). *Vehicle Motion Engineering Compendium.* `https://research.chalmers.se/en/publication/543173`

[7] Weyburne, D. Own work.

[8] Cleynen, O. Own work.

[9] Josefsson, E., & Hagvall, R., & Urquhart, M., & Sebben, S. (2018). *Numerical Analysis of Aerodynamic Impact on Passenger Vehicles during Cornering.* SAE Technical Paper 2018-37-0014, 2018, doi:10.4271/2018-37-0014.

[10] Schuetz, T. C. (2015). *Aerodynamics of Road Vehicles, Fifth Edition.*

[11] Nayman, M. & Penny, C. (2020). *Developing Steady-State Cornering CFD Simulations for Use in FSAE.* Work done in conjunction with Siemens and Queen's Formula SAE.

[12] *FSG Timekeeping.* `https://tk.formulastudent.de/internet/skidpad?discipline_id=skidpad&discipline_name=Skidpad`

DEPARTMENT OF MECHANICS AND MARITIME SCIENCES
CHALMERS UNIVERSITY OF TECHNOLOGY
Gothenburg, Sweden 2025
www.chalmers.se

CHALMERS
UNIVERSITY OF TECHNOLOGY